Nuclear Science and Techniques (2024) 35:190
https://doi.org/10.1007/s41365-024-01535-w

Reduced-order method for nuclear reactor primary circuit calculation

Ze-Long Zhao[1] · Ya-Hui Wang[1] · Zhe-Xian Liu[1] · Hong-Hang Chi[1] · Yu Ma[1]

Received: 18 December 2023 / Revised: 6 February 2024 / Accepted: 23 March 2024 / Published online: 9 October 2024

Abstract
Accurate real-time simulations of nuclear reactor circuit systems are particularly important for system safety analysis and design. To effectively improve computational efficiency without reducing accuracy, this study establishes a thermal-hydraulics reduced-order model (ROM) for nuclear reactor circuit systems. The full-order circuit system calculation model is first established and verified and then used to calculate the thermal-hydraulic properties of the circuit system under different states as snapshots. The proper orthogonal decomposition method is used to extract the basis functions from snapshots, and the ROM is constructed using the least-squares method, effectively reducing the difficulty in constructing the ROM. A comparison between the full-order simulation and ROM prediction results of the AP1000 circuit system shows that the proposed ROM can improve computational efficiency by 1500 times while achieving a maximum relative error of 0.223%. This research develops a new direction and perspective for the digital twin modeling of nuclear reactor system circuits.

Keywords Reactor system model · Primary circuit · Reduced-order · Proper orthogonal decomposition · Least-squares method

1 Introduction

Simulations of nuclear reactor circuit systems provide a versatile and intuitive tool to understand their operating mechanisms and performances, including their thermal-hydraulic properties [1–3], safety features [4, 5], and operational efficiency [6]. To analyze the detailed thermal-hydraulic behavior in the reactor core circuit, the computational fluid dynamics (CFD) [7] method has been adopted in pressurized water reactors (PWRs) [8] and boiling water reactors [9], which solves the Navier–Stokes equations, large-eddy simulation equations, and Reynolds-averaged Navier–Stokes equations to simulate the flow and heat transfer phenomena inside the circuit in detail. However, because the simulation of a nuclear reactor circuit system involves large-scale multiphysics coupling calculations, real-time and ultra-real-time CFD simulations are challenging [10]. For the simulation of a full-circuit system, a coarse-mesh average distribution is often sufficient for engineering requirements. From this perspective, various simplified methods have been developed, including lumped parameter models [11], subchannel analysis [12], nodal methods [13], and the one-dimensional finite difference method (FDM) [14]. These studies have effectively supported the steady-state analysis [15], transient response [16, 17], and controller design [18] of Generation III reactor systems [19]. Simultaneously, they have provided significant assistance in the thermal-hydraulic analysis [20, 21], core design, and economic-benefit assessment [22] of Generation IV reactor systems [23].

Although these system programs can quickly achieve an accurate simulation of the entire circuit system, their computational efficiency still requires further improvement for real-time simulations, and especially for ultra-real-time simulations, which is particularly important for digital twins and data assimilation [24, 25]. In these applications, numerical simulations need to be synchronized with actual operating conditions or should be faster than actual operating

This work is supported by the National Natural Science Foundation of China (No. 12205389), Guangdong Basic and Applied Basic Research Foundation (No. 2022A1515011735), and Science and Technology on Reactor System Design Technology Laboratory (No. KFKT-05-FWHT-WU-2023014).

✉ Ya-Hui Wang
wangyh296@mail.sysu.edu.cn

✉ Yu Ma
mayu9@mail.sysu.edu.cn

[1] Sino-French Institute of Nuclear Engineering and Technology, Sun Yat-sen University, Zhuhai 519082, China

conditions to simulate physical phenomena inside the circuit so that operators can carry out their corresponding operations. Therefore, for both commercial nuclear power plants and research reactors, establishing an accurate real-time or ultra-real-time simulation platform [23] is of paramount importance. In particular, when applied to power plant condition monitoring and fault diagnosis, an efficient and accurate numerical method can provide data support for the data assimilation process [24]. Therefore, reduced-order methods (ROMs) [26–29] may be an efficient approach.

The ROM constitutes an approach that can significantly reduce computational resource requirements and processing time. This target is achieved by generating snapshots from preexisting data, extracting data characteristics from these snapshots, and subsequently employing these data characteristics to make accurate and efficient predictions of unknown conditions. Several ROMs have been proposed and applied to various engineering disciplines. The Routh approximation method was proposed in the field of order reduction for linear time-invariant systems [30]. Reduced-order modeling of large-scale dynamical systems has been achieved with the application of Krylov subspace methods [31]. Furthermore, linear system reduction techniques such as the Pade approximation method have been employed, as demonstrated by [32]. Moreover, proper orthogonal decomposition (POD) has garnered widespread use in fluid-dynamic analyses [33] and the characterization of coherent features within fluid flows [34]. Sartori et al. [35] employed POD theory to investigate the single-channel model of a lead-cooled fast reactor. It also demonstrated efficacy in solving parameterized nonlinear partial differential equations [36], yielding commendable results in various applications.

This study aims to establish a POD-ROM for modeling reactor primary circuit systems to accelerate thermal-hydraulic calculations and maintain accuracy. The remainder of this paper is organized as follows: In Sect. 2, the theoretical foundations of the primary circuit full-order model theory, POD reduced-order theory, and circuit reduced-order model theory are explained. In Sect. 3, we present the outcomes of computations conducted with both full- and reduced-order models under diverse operating conditions. These results were subjected to meticulous analysis and discussion, encompassing an examination of the relative errors between them. Finally, Sect. 4 presents the concluding remarks of this study.

2 Modeling theory

2.1 Full-order model

This section introduces the modeling theory of a one-dimensional steady-state thermal system circuit. An AP1000 reactor [37] is used as an example. This intricate circuit comprises essential components, namely, the reactor core, pressurizer, steam generator, and pump, all interconnected through a pipe model representation. Notably, the pressurizer serves as a pressure-containment boundary within this circuit, maintaining a constant pressure of 15.5 MPa [38]. The main pump model is based on the nuclear main pump head normalization curve provided by Zhu et al. [39], where the rated head of the AP1000 reactor coolant pump is 111.3 m, and the design mass flow rate is 17,886 (m^3/h). The spatial arrangement of these critical components and interconnecting pipes is shown in Fig. 1 for reference.

The proposed method is divided into two stages: offline and online. For the offline stage, the one-dimensional FDM for solving system thermal-hydraulic equations is first employed as a full-order numerical method to model the thermal-hydraulic behavior of components within the primary circuit system. A series of typical samples of the circuit calculation results under different states from the full-order model were chosen as snapshots to generate a reduced-order model of the primary thermal system circuit (RO-PTSC). In the online stage, the proposed reduced-order model can be used to simulate the thermal-hydraulic properties with significant acceleration and high accuracy. The intricate process of constructing this reduced-order model is illustrated in Fig. 2, providing a visual representation of our methodology.

2.1.1 Core

The reactor core generates heat via nuclear fission, which is the primary energy source for nuclear power systems. The thermal-hydraulic process for the reactor core is characterized by a single-channel model [40], which describes a one-dimensional distribution along the axial direction. The governing equations

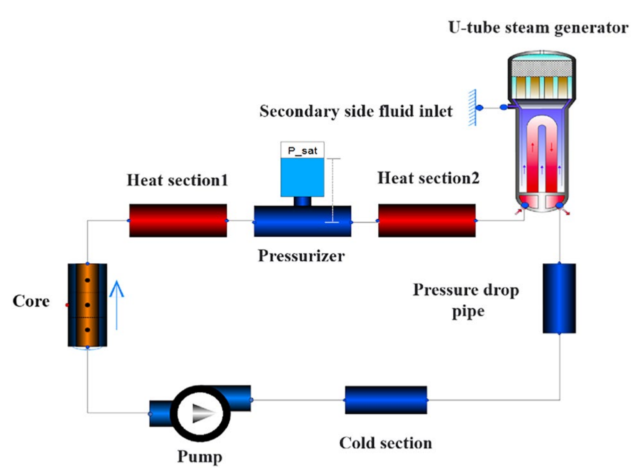

Fig. 1 (Color online) Primary circuit schematic of the AP1000 reactor

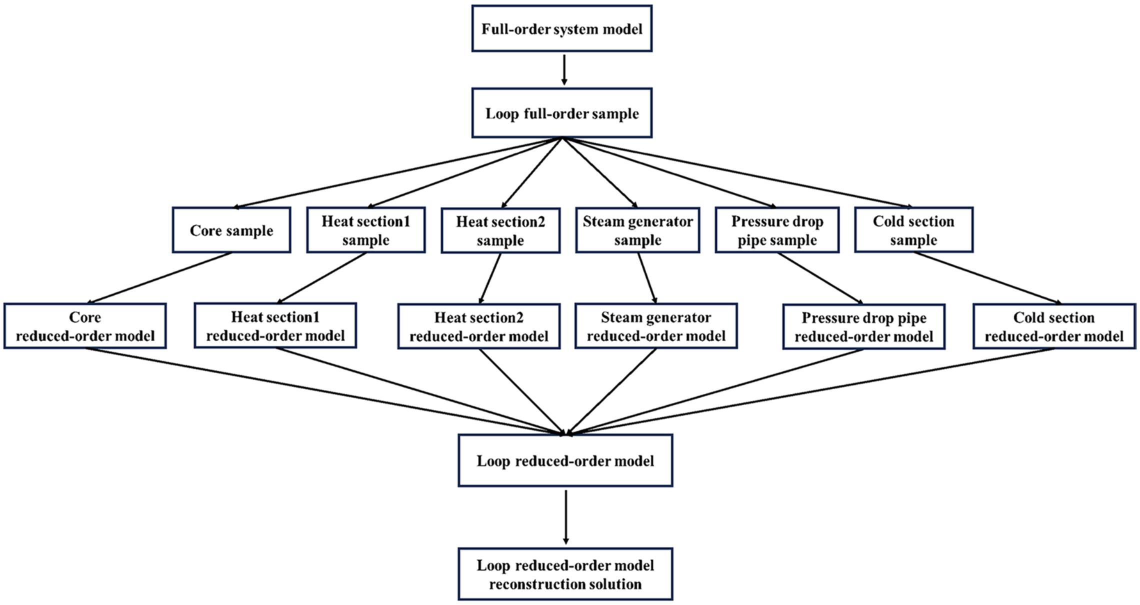

Fig. 2 Flowchart of RO-PTSC model construction

of this model include the continuity, momentum, and energy equations, as follows:

$$\frac{\mathrm{d}(\rho u)}{\mathrm{d}x} = 0, \tag{1}$$

$$\frac{\mathrm{d}(\rho uu)}{\mathrm{d}x} = \frac{\mathrm{d}}{\mathrm{d}x}\left(\mu\frac{du}{dx}\right) - \frac{\mathrm{d}P}{\mathrm{d}x} - \frac{\rho u^2}{2}\left(\frac{f}{D} + \frac{K_{\mathrm{sp}}}{\Delta x}\right) - \rho g, \tag{2}$$

$$\frac{\mathrm{d}(\rho uh + pu)}{\mathrm{d}x} = \frac{\mathrm{d}}{\mathrm{d}x}\left(\lambda\frac{\mathrm{d}T}{\mathrm{d}x}\right) + q_{\mathrm{c}}, \tag{3}$$

where ρ represents the fluid density (kg/m^3); x represents the axial coordinate along the core (m); u is the flow velocity (m/s); μ represents the dynamic viscosity (Pa s); p represents the pressure (Pa); f represents the Darcy friction coefficient; D represents the equivalent diameter of the reactor core (m) according to the coolant flow rate; K_{sp} represents the form-resistance pressure drop coefficient; Δx denotes the unit node length (m); g represents the gravitational acceleration (m/s^2); T is the temperature (K); h is the specific enthalpy (J/(kg)); λ represents the thermal conductivity (W/(m K)); q represents the heat absorbed per unit volume of coolant (W/m^3), which can be written as $q = Q/V_{\mathrm{g}}$, where V_{g} represents the per-unit node volume (W/m^3); and Q represents the thermal power (W). For FDM discretization, the thermal power of the ith control element is calculated as $Q_i = Q_{\mathrm{c}}\phi_i / \sum_{i=1}^{NX_{\mathrm{c}}} \phi_i$, where Q_{c} represents the core total power (W); NX_{c} denotes the discrete number of cores in the axial direction; and ϕ denotes the neutron flux (1/(m^2 s)). The equation for the friction factor f can be written as

$$f = \max\left\{ \begin{array}{c} 64/Re, \\ 0.0055\left(1 + \left(20000\frac{\varepsilon}{D} + \frac{10^6}{Re}\right)^{1/3}\right) \end{array} \right\}, \tag{4}$$

where ε represents the roughness (m), and Re denotes the Reynolds number.

The form-resistance pressure drop coefficient K_{sp} is expressed as follows [41]:

$$K_{\mathrm{sp}} = C_{\mathrm{VD}}\xi^2, \tag{5}$$

where ξ represents the ratio of the flow area of the positioning grid to that of the bar bundle, and C_{VD} represents the modified drag coefficient, which can be written as

$$C_{\mathrm{VD}} = 3.5 + \left(\frac{73.14}{\mathrm{Re}^{0.264}}\right) + \left(\frac{2.79\times 10^{10}}{\mathrm{Re}^{2.79}}\right). \tag{6}$$

2.1.2 Pipe

Two types of distinct pipe models are introduced in this context. The first model is the discrete pressure drop pipe model, which does not consider heat transfer. Conversely, the second model is the discrete heat transfer pipe model, which explicitly accounts for heat transfer effects [42]. The governing equations for the discrete pressure drop pipe model include the continuity and momentum equations, which are given by the following equations:

$$\frac{\mathrm{d}(\rho u)}{\mathrm{d}x} = 0, \tag{7}$$

$$\frac{\mathrm{d}(\rho u u)}{\mathrm{d}x} = \frac{\mathrm{d}}{\mathrm{d}x}\left(\mu \frac{\mathrm{d}u}{\mathrm{d}x}\right) - \frac{\mathrm{d}p}{\mathrm{d}x} - \frac{1}{2}\frac{f_{\mathrm{p}}}{d}\rho u^2 - \rho g \sin\theta, \tag{8}$$

where θ represents the pipe tilt angle, and d represents the inner diameter of the pipe (m). f_{p} represents the Darcy friction factor in the pipes, which can be expressed as [43]:

$$\begin{cases} f_{\mathrm{p}} & = \frac{64}{Re}, Re_{\mathrm{D}} \le Re_{\mathrm{cr}} \\ \frac{1}{f_{\mathrm{p}}^{1/2}} & = -2\log\left(\frac{\varepsilon_{\mathrm{p}}/d}{3.7} + \frac{2.51}{Re_{\mathrm{D}} f_{\mathrm{p}}^{1/2}}\right), Re_{\mathrm{D}} > Re_{\mathrm{cr}} \end{cases} \tag{9}$$

where Re_{D} is the pipe Reynolds number, Re_{cr} is the critical Reynolds number, and ε_{p} is the pipe roughness (m).

In the discrete heat transfer pipe model, an energy equation must be incorporated into the continuity and momentum equations. The energy equations can be expressed as follows:

$$\frac{\mathrm{d}(\rho u h)}{\mathrm{d}x} = \frac{\mathrm{d}}{\mathrm{d}x}\left(\lambda \frac{\mathrm{d}T}{\mathrm{d}x}\right) + q_{\mathrm{p}}, \tag{10}$$

where q_{p} denotes volumetric heat release rate (W/m^3).

2.1.3 Steam generator

The steam generator is the interface between the primary and second circuits, where the coolant of the primary circuit flows through the U-tube and transfers heat to the coolant of the second circuit. To simulate this equipment, the one-dimensional dynamic mathematical model proposed by Zhang et al. [44] is adopted, which introduces a distributed parameter model tailored for steam generators in PWRs. As shown in Fig. 3, $T_{1,\mathrm{f}}$ and $T_{1,\mathrm{ad}}$ represent the fluid temperature of the primary side in the parallel and counter-flow sections, respectively. $T_{\mathrm{w,in,f}}$ and $T_{\mathrm{w,out,f}}$ represent the inner and outer wall temperatures of the U-tube in the parallel flow section, respectively. $T_{\mathrm{w,in,ad}}$ and $T_{\mathrm{w,out,ad}}$ represent the inner and outer wall temperatures of the U-tube in the counter-flow section, respectively. $T_{2,\mathrm{r}}$ and $T_{2,\mathrm{s}}$ represent the preheating and boiling section temperatures of the secondary side fluid, respectively. $T_{1,\mathrm{in}}$ represents the inlet temperature on the primary side, $T_{2,\mathrm{in}}$ is the inlet temperature on the secondary side, and $T_{1,\mathrm{out}}$ represents the outlet temperature on the primary side.

The steady-state heat dynamic balance equations of the parallel and counter-flows of the primary side can be written as follows:

$$\frac{m_1}{M_1}\frac{\mathrm{d}T_{1,\mathrm{f}}}{\mathrm{d}x} = \frac{n\pi d_{\mathrm{in}} K_1}{M_1 c_{\mathrm{p,f}}}(T_{\mathrm{w,in,f}} - T_{1,\mathrm{f}}), \tag{11}$$

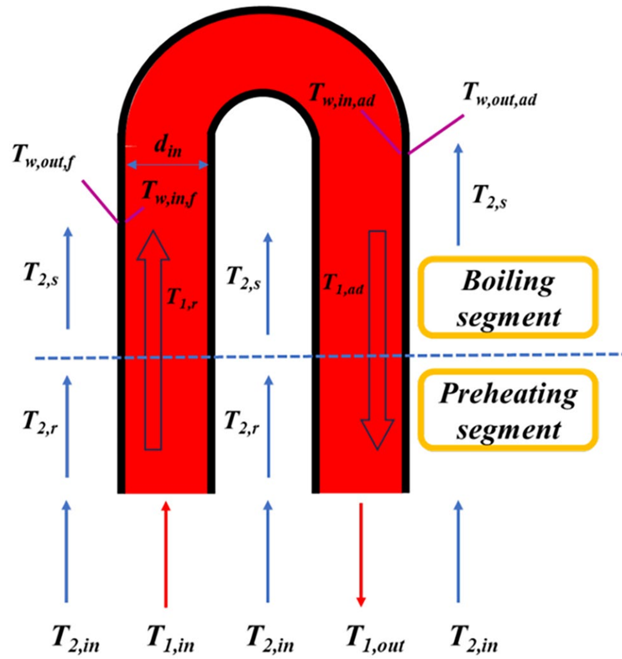

Fig. 3 One-dimensional dynamic model of steam generators

$$\frac{m_1}{M_1}\frac{\mathrm{d}T_{1,\mathrm{ad}}}{\mathrm{d}x} = -\frac{n\pi d_{\mathrm{in}} K_1}{M_1 c_{\mathrm{p,ad}}}(T_{\mathrm{w,in,ad}} - T_{1,\mathrm{ad}}), \tag{12}$$

in which m_1 is the mass flow rate of the primary side (kg/s) defined as $m_1 = \frac{n}{4}\pi\rho_1 u_1 d_{\mathrm{in}}^2$, and ρ_1 and u_1 are the density (kg/m^3) and velocity (m/s) of the primary side coolant, respectively; M_1 represents the fluid mass per unit length along the axial direction of the primary side (kg/m) and is defined as $M_1 = \frac{n}{4}\pi\rho_1 d_{\mathrm{in}}^2$; n is the number of heat transfer tubes; d_{in} denotes the inner diameter of the U-tubes; $c_{\mathrm{p,f}}$ represents the constant-pressure specific heat capacity of the coolant on the primary side (J/(kg K)); and K_1 represents the average heat transfer coefficient of the primary side (W/(m^2 K)), which can be written using the Dittus–Boelter formula [45]:

$$K_1 = 0.023\frac{\lambda_1}{d_{\mathrm{in}}} Re_1^{0.8} Pr_1^{0.3}, \tag{13}$$

where λ_1 denotes the fluid thermal conductivity on the primary side (W/(m K)). Re_1 and Pr_1 are the Reynolds and Prandtl numbers on the primary side, respectively.

The heat-balance equations of the U-tube inner wall for parallel and counter-flows can be written as

$$\frac{2n\pi\lambda_{\mathrm{w}}}{M_{\mathrm{w}}c_{\mathrm{p,w}}\ln(d_{\mathrm{out}}/d_{\mathrm{in}})}(T_{\mathrm{w,out,f}}-T_{\mathrm{w,in,f}}) + \frac{nK_1\pi d_{\mathrm{in}}}{M_{\mathrm{w}}c_{\mathrm{p,w}}}(T_{1,\mathrm{f}}-T_{\mathrm{w,in,f}})=0, \tag{14}$$

$$\frac{2n\pi\lambda_{\mathrm{w}}}{M_{\mathrm{w}}c_{\mathrm{p,w}}\ln(d_{\mathrm{out}}/d_{\mathrm{in}})}(T_{\mathrm{w,out,ad}}-T_{\mathrm{w,in,ad}}) + \frac{nK_1\pi d_{\mathrm{in}}}{M_{\mathrm{w}}c_{\mathrm{p,w}}}(T_{1,\mathrm{ad}}-T_{\mathrm{w,in,ad}})=0, \tag{15}$$

where $c_{\mathrm{p,w}}$ is the constant-pressure specific heat capacity of the U-tube wall (J/(kg K)); λ_{w} is the thermal conductivity of the wall (W/(m K)); d_{out} denotes the outer diameter of the U-tube (m); and M_{w} denotes the tube wall mass per unit length in the axial direction (kg/m).

The heat-balance equations of the outer wall of the U-tube for the parallel flow in the preheating and boiling sections can be written as follows:

$$\frac{2n\pi\lambda_{\mathrm{w}}}{M_{\mathrm{w}}c_{\mathrm{p,w}}\ln(d_{\mathrm{out}}/d_{\mathrm{in}})}(T_{\mathrm{w,in,f}}-T_{\mathrm{w,out,f}}) + \frac{nK_2\pi d_{\mathrm{out}}}{M_{\mathrm{w}}c_{\mathrm{p,w}}}(T_{2,\mathrm{r}}-T_{\mathrm{w,out,f}})=0, \tag{16}$$

$$\frac{2n\pi\lambda_{\mathrm{w}}}{M_{\mathrm{w}}c_{\mathrm{p,w}}\ln(d_{\mathrm{out}}/d_{\mathrm{in}})}(T_{\mathrm{w,in,f}}-T_{\mathrm{w,out,f}}) + \frac{nK_{2,\mathrm{s}}\pi d_{\mathrm{out}}}{M_{\mathrm{w}}c_{\mathrm{p,w}}}(T_{2,\mathrm{s}}-T_{\mathrm{w,out,f}})=0. \tag{17}$$

Similarly, the heat-balance equation of the outer wall of the U-tube for the counter-flow of the preheating and boiling sections can be written as

$$\frac{2n\pi\lambda_{\mathrm{w}}}{M_{\mathrm{w}}c_{\mathrm{p,w}}\ln(d_{\mathrm{out}}/d_{\mathrm{in}})}(T_{\mathrm{w,in,ad}}-T_{\mathrm{w,out,ad}}) + \frac{nK_2\pi d_{\mathrm{out}}}{M_{\mathrm{w}}c_{\mathrm{p,w}}}(T_{2,\mathrm{r}}-T_{\mathrm{w,out,ad}})=0, \tag{18}$$

$$\frac{2n\pi\lambda_{\mathrm{w}}}{M_{\mathrm{w}}c_{\mathrm{p,w}}\ln(d_{\mathrm{out}}/d_{\mathrm{in}})}(T_{\mathrm{w,in,ad}}-T_{\mathrm{w,out,ad}}) + \frac{nK_{2,\mathrm{s}}\pi d_{\mathrm{out}}}{M_{\mathrm{w}}c_{\mathrm{p,w}}}(T_{2,\mathrm{s}}-T_{\mathrm{w,out,ad}})=0, \tag{19}$$

where K_2 and $K_{2,\mathrm{s}}$ denote the heat transfer coefficients of the preheating and boiling sections of the secondary side, respectively.

In a natural-circulation steam generator, the heat transfer process in the preheating section of the secondary side undergoes supercooled boiling. Therefore, the convection heat transfer coefficient in the preheating section can be uniformly treated by following the approach used for the boiling section and the principles of boiling heat transfer. According to Rohsenow [46], the heat transfer coefficient can be described as follows:

$$K_2=\frac{c_{\mathrm{p,s}}}{C_{\mathrm{w}}\gamma\mathrm{Pr}_{\mathrm{s}}^{m}}q^{\frac{2}{3}}\cdot\left[\mu_{\mathrm{s}}\gamma\sqrt{\frac{g(\rho_{\mathrm{s}}-\rho_{\mathrm{g}})}{\sigma}}\right]^{\frac{1}{3}}, \tag{20}$$

where $c_{\mathrm{p,s}}$ is the constant-pressure specific heat capacity of saturated water (J/(kg K)); C_{w} is the combination factor of a particular heating surface fluid; Pr_{s} represents the Prandtl number of saturated water; m is an empirical index, for water, m=1; μ_{s} represents the viscosity of saturated water (kg/(m s)); γ denotes the latent heat of vaporization (kJ/kg); g represents the gravitational acceleration (m/s^2); ρ_{s} represents the density of saturated water (kg/m^3); ρ_{g} is the density of saturated steam (kg/m^3); σ represents the surface tension of water at the vapor–liquid interface (W/m^2); and q denotes the heat-flow density on the secondary side (W/m^2).

The heat-balance equations of the preheating and boiling sections of the secondary side are as follows:

$$\frac{m_2}{M_2}\frac{\mathrm{d}T_{2,\mathrm{r}}}{\mathrm{d}x}=\frac{n\pi d_{\mathrm{out}}K_2}{M_2c_{\mathrm{p,2}}}(T_{\mathrm{w,out,f}}+T_{\mathrm{w,out,ad}}-2T_{2,\mathrm{r}}), \tag{21}$$

$$\frac{m_2}{M_2}\frac{\mathrm{d}h_{2,\mathrm{s}}}{\mathrm{d}x}=\frac{n\pi d_{\mathrm{out}}K_{2,\mathrm{s}}}{M_2}(T_{\mathrm{w,out,f}}+T_{\mathrm{w,out,ad}}-2T_{2,\mathrm{s}}), \tag{22}$$

where $c_{\mathrm{p,2}}$ represents the constant-pressure specific heat capacity of the fluid-preheating section on the secondary side (J/(kg K)); M_2 represents the fluid mass per unit length along the axial direction of the secondary side preheating section (kg/m); and $h_{2,\mathrm{s}}$ is the enthalpy of the boiling section on the secondary side (J/kg).

2.1.4 Connection between different components

The primary circuit comprises the above components, all connected. Mathematically, this connection is achieved by transferring physical quantities between different component equations, as shown in Fig. 4.

In Fig. 4, the inlet and outlet of each component are represented by dashed-line and dashed-dotted-line boxes, respectively. Along the yellow arrows, the output variables of each component, including temperature, pressure, and velocity, are transferred to the next component as input values. For example, the output temperature, pressure, and velocity of the core are transferred to heat section 1 as inlet variables.

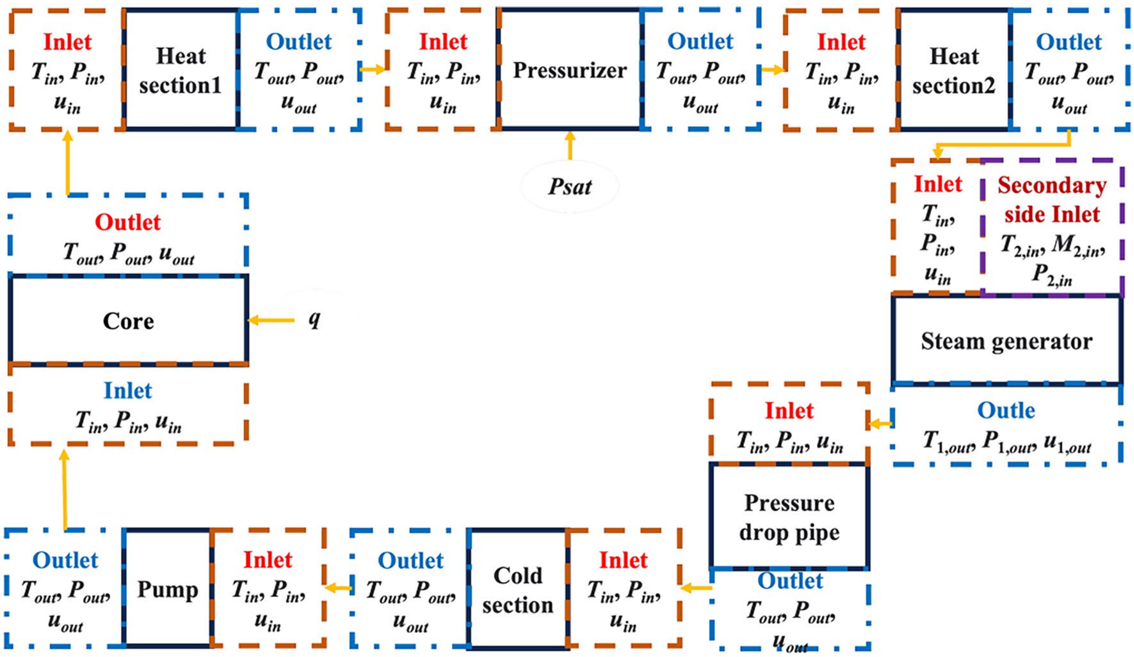

Fig. 4 Connection between different components

2.1.5 Numerical computation methods of the full-order model

The AP1000 primary circuit model constructed in this study comprises a core, heat section, pressurizer, steam generator, pressure drop pipe, cold section, and pump, as shown in Fig. 1. Among these components, the physical field distributions in the core, heat section, steam generator, pressure drop pipe, and cold section are computed using the FDM. The calculated area is discretized using a uniform mesh configuration along the coolant flow direction. The physical properties of the coolant, including thermal conductivity, density, kinematic viscosity, and specific heat capacity, are defined as functions of temperature and pressure based on the IF97 thermophysical property table [47].

In the governing equations of the pipes and cores, the convective terms are discretized using the first-order upwind scheme [48], whereas the diffusion terms are discretized using a central differencing scheme [49]. The discretization formats of the governing equations for both the pipes and reactor core can be expressed as follows, where i represents the index of the internal grids and the subscripts 'p' and 'c' represent the pipe and core, respectively. Continuity equation:

$$\frac{(\rho u)_{\mathrm{p},i} - (\rho u)_{\mathrm{p},i-1}}{\Delta x_{\mathrm{p}}} = 0, \tag{23}$$

$$\frac{(\rho u)_{\mathrm{c},i} - (\rho u)_{\mathrm{c},i-1}}{\Delta x_{\mathrm{c}}} = 0. \tag{24}$$

Momentum equation:

$$\begin{aligned} \frac{(\rho uu)_{\mathrm{p},i} - (\rho uu)_{\mathrm{p},i-1}}{\Delta x_{\mathrm{p}}} &= \frac{1}{\Delta x_{\mathrm{p}}}\left(\frac{(\mu u)_{\mathrm{p},i+1} - 2(\mu u)_{\mathrm{p},i} + (\mu u)_{\mathrm{p},i-1}}{\Delta x_{\mathrm{p}}}\right) \\ &- \frac{p_{\mathrm{p},i} - p_{\mathrm{p},i-1}}{\Delta x_{\mathrm{p}}} - \frac{f_{\mathrm{p}}}{2d}\rho_{\mathrm{p},i}u^2_{\mathrm{p},i} \\ &- \rho_{\mathrm{p},i} g \sin\theta, \end{aligned} \tag{25}$$

$$\begin{aligned} \frac{(\rho uu)_{\mathrm{c},i} - (\rho uu)_{\mathrm{c},i-1}}{\Delta x_{\mathrm{c}}} &= \frac{1}{\Delta x_{\mathrm{c}}}\left(\frac{(\mu u)_{\mathrm{c},i+1} - 2(\mu u)_{\mathrm{c},i} + (\mu u)_{\mathrm{c},i-1}}{\Delta x_{\mathrm{c}}}\right) \\ &- \frac{p_{\mathrm{c},i} - p_{\mathrm{c},i-1}}{\Delta x_{\mathrm{c}}} - \frac{1}{2}\left(\frac{f}{D} + \frac{K_{\mathrm{sp}}}{\Delta x_{\mathrm{c}}}\right)\rho_{\mathrm{c},i}u^2_{\mathrm{c},i} \\ &- \rho_{\mathrm{c},i} g. \end{aligned} \tag{26}$$

Energy equation:

$$\frac{(\rho uh)_{\mathrm{p},i}-(\rho uh)_{\mathrm{p},i-1}}{\Delta x_{\mathrm{p}}} = \frac{1}{\Delta x_{\mathrm{p}}}\left(\frac{(\lambda T)_{\mathrm{p},i+1}-2(\lambda T)_{\mathrm{p},i}+(\lambda T)_{\mathrm{p},i-1}}{\Delta x_{\mathrm{p}}}\right) + q_{\mathrm{p},i}, \tag{27}$$

$$\frac{(\rho uh)_{\mathrm{c},i}-(\rho uh)_{\mathrm{c},i-1}+(pu)_{\mathrm{c},i}-(pu)_{\mathrm{c},i-1}}{\Delta x_{\mathrm{c}}} = \frac{1}{\Delta x_{\mathrm{c}}}\left(\frac{(\lambda T)_{\mathrm{c},i+1}-2(\lambda T)_{\mathrm{c},i}+(\lambda T)_{\mathrm{c},i-1}}{\Delta x_{\mathrm{c}}}\right) + q_{\mathrm{c},i}. \tag{28}$$

The inlet boundaries for the temperature, flow velocity, and pressure are applied to the inlet of the pipes and core, and the fully developed boundaries for the outlet boundaries are applied to the pipes and core [50].

For the governing equations of the steam generator, the discretization of Eqs. (11), (12), (21), and (22) employs a first-order upwind scheme, which is written as follows:

$$\frac{m_1}{M_1}\frac{\left(T_{1,\mathrm{f},i}-T_{1,\mathrm{f},i-1}\right)}{\Delta x_{\mathrm{SG}}} = \frac{n\pi d_{\mathrm{in}}K_1}{M_1 c_{\mathrm{p,f}}}(T_{\mathrm{w,in,f}}-T_{1,\mathrm{f}}), \tag{29}$$

$$\frac{m_1}{M_1}\frac{\left(T_{1,\mathrm{ad},i+1}-T_{1,\mathrm{ad},i}\right)}{\Delta x_{\mathrm{SG}}} = -\frac{n\pi d_{\mathrm{in}}K_1}{M_1 c_{\mathrm{p,ad}}}(T_{\mathrm{w,in,ad}}-T_{1,\mathrm{ad}}), \tag{30}$$

$$\frac{m_2}{M_2}\frac{\left(T_{2,\mathrm{r},i}-T_{2,\mathrm{r},i-1}\right)}{\Delta x_{\mathrm{SG}}} = \frac{n\pi d_{\mathrm{out}}K_2}{M_2 c_{\mathrm{p},2}}(T_{\mathrm{w,out,f}}+T_{\mathrm{w,out,ad}}-2T_{2,\mathrm{r}}), \tag{31}$$

$$\frac{m_2}{M_2}\frac{\left(h_{2,\mathrm{s},i}-h_{2,\mathrm{s},i-1}\right)}{\Delta x_{\mathrm{SG}}} = \frac{n\pi d_{\mathrm{out}}K_{2,\mathrm{s}}}{M_2}(T_{\mathrm{w,out,f}}+T_{\mathrm{w,out,ad}}-2T_{2,\mathrm{s}}). \tag{32}$$

The inlet boundary conditions for temperature and enthalpy are applied to the primary and secondary sides of the steam generator. On the secondary side, the inlet temperature is defined as the corresponding coolant inlet temperature of the core, whereas the outlet boundary is set as a fully developed boundary.

2.2 Reduced-order model

2.2.1 Snapshots and POD bases

As previously mentioned, the construction of the reduced-order model involves offline and online stages, as shown in Fig. 5. In the offline stage, the full-order model is used to generate snapshots under various typical operating conditions. In the online stage, the reduced-order model is applied to predict the distributions of temperature, velocity, and pressure for unknown states. The first step in the offline stage is to calculate snapshots of different operation states, including the temperature, pressure, and velocity distributions. During this process, N operating states are selected within the operating range, and snapshots of these states are calculated using the full-order model (FOM) described in Sect. 2.1. The snapshot set generated in the offline stage based on the FOM is expressed as follows:

$$A = \left[\alpha_1, \alpha_2, \ldots, \alpha_h, \ldots, \alpha_N\right], \tag{33}$$

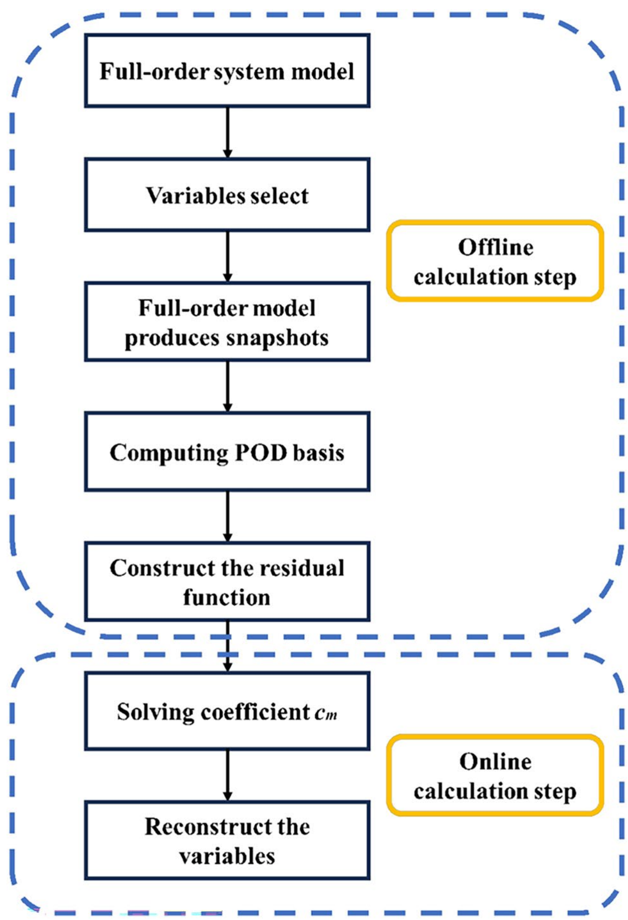

Fig. 5 Reduced-order calculation steps

where α_h represents the variation set at the hth operation condition, which can be expressed as

$$\alpha_h = \left[\alpha_{h,1}, \dots, \alpha_{h,k}, \dots, \alpha_{h,L}\right]^{\mathrm{T}}, \tag{34}$$

where k is the kth variable, and L is the total number of variables. Within the primary circuit, NX grids are set for the numerical calculation, and $\alpha_{h,k}$ can be expressed as follows:

$$\alpha_{h,k} = \left[\alpha_{h,k,1}, \dots, \alpha_{h,k,g}, \dots, \alpha_{h,k,NX}\right]^{\mathrm{T}}, \tag{35}$$

where g represents the gth discrete grid, and $\alpha_{h,k,g}$ represents the value of the kth variable at the gth grid under the hth operation condition.

The main modes of the system variation, namely the POD bases, can be extracted based on a thorough analysis and processing of these snapshots, thereby realizing the objective of reducing the system intricacy to a lower-dimensional representation. POD bases consist of a set of modes or functions employed to characterize the predominant characteristics of variation within a system. These modes are extracted from snapshots and are conventionally represented as feature vectors. According to POD theory [51], the POD basis can be obtained from the eigenvalues and eigenvectors of the matrix S, which can be expressed as follows:

$$S = A^{\mathrm{T}}A. \tag{36}$$

The eigenvalues of S are defined as λ_i, $i \in [\![1, N]\!]$, which satisfy $\lambda_1 > \cdots > \lambda_i > \cdots > \lambda_N > 0$. The corresponding eigenvectors of these eigenvalues are $X_1, \dots, X_i, \dots, X_N$, and the POD basis P_m can be defined as follows:

$$P_m = \frac{1}{\sqrt{\lambda_m}} A X_m, \quad m = 1, 2, \dots, N \tag{37}$$

$$P_m = \begin{bmatrix} P_{m,1,1}, \dots, P_{m,1,g}, \dots, P_{m,1,NX}, \dots \\ P_{m,k,1}, \dots, P_{m,k,g}, \dots, P_{m,k,NX}, \dots \\ P_{m,L,1}, \dots, P_{m,L,g}, \dots, P_{m,L,NX}, \dots \end{bmatrix}^{\mathrm{T}}, \tag{38}$$

where $P_{m,k,g}$ represents the m-order POD basis corresponding to variable kth at the gth grid.

As the governing equations and snapshots generated by the full-order model for each component are different, special POD bases are formed for different components. In addition, for the same type of pipe, although the governing equations remain the same, different positions in the circuit result in different diameters and lengths. Consequently, their snapshots and generated POD bases are different.

According to POD theory, the significance of eigenvectors is directly associated with the magnitude of their corresponding eigenvalues. To determine the POD order N_p for reduced-order modeling, the following criteria can be used:

$$\begin{cases} N_p = \arg\min \left\{ I(N_p) : I(N_p) \geq 1 - 10^{-8} \right\}, \\ I(N_p) = \dfrac{\sum_{i=1}^{N_p} \lambda_i}{\sum_{i=1}^{N} \lambda_i}, \end{cases} \tag{39}$$

where $I(N_p)$ denotes the energy fraction of the first N_p POD mode. Subsequently, the snapshots $\alpha_{h',k,g}$ can be expanded as

$$\alpha_{h',k,g} = \sum_{m=1}^{N_p} c_m P_{k,g,m}, \tag{40}$$

where c_m is the mth-order basis function coefficient. Therefore, in the process of solving a one-dimensional thermal circuit system, POD bases can be effectively applied to reconstruct the temperature, pressure, velocity, and relevant variables throughout the entire circuit under various operating conditions. The main task for the following processes is to establish the reduced-order model for solving the basis function coefficient c_m, which, in this work, is achieved using the least-squares method (LSM) [52]. The main purpose of the ROM based on the LSM is to substitute Eq. (40) into linear equations (23)–(32). The residual functions of these equations are constructed as

$$E = \sum_i \sum_m A_i c_m P_{i,m} - b_i, \tag{41}$$

where the subscripts i and m represent the indices of the mesh and POD order, respectively. A and b represent the stiffness matrix and source vector of the linear system, respectively.

The operating conditions to be predicted, including the inlet temperature, inlet flow rate, and core power, can be

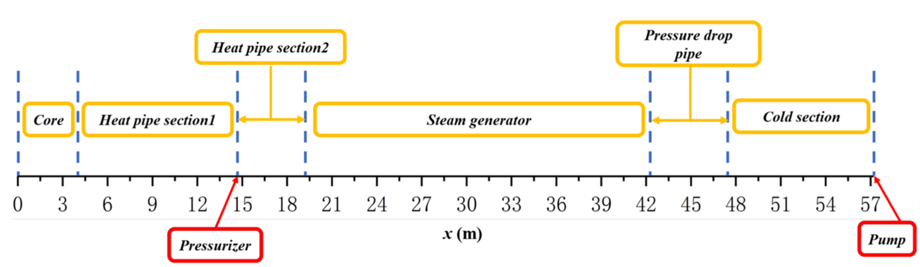

Fig. 6 Distribution of components along the flow direction

introduced by imposing the corresponding data at node i. For example, the flow rate of inlet node i is set to the given inlet value.

When using the LSM, the POD coefficient c_m can be determined by minimizing the residual equation, which converts Eq. (41) to the following equations:

$$\frac{\partial E}{\partial c_m} = 0, \quad m = 1, 2, \ldots \tag{42}$$

After determining c_m, the distribution variables, such as temperature, velocity, and pressure, can be obtained using Eq. (40). In the following section, the reduced-order model, mainly the residual functions of the primary circuit, is described in detail.

2.2.2 Primary circuit POD reduced-order model

To construct an entire reduced-order model for the primary circuit of the reactor, reduced-order models of the primary components within the circuit must first be established. For the AP1000 primary circuit considered in this study, the components primarily encompassed the core, pipes, and steam generator. Other components with relatively minor effects on computational efficiency, such as regulators and pumps, do not require the development of reduced-order models. The spatial arrangement of AP1000 primary circuit components along the coolant traversing distance is shown in Fig. 6.

As previously mentioned, the establishment of the reduced-order model is based on a collection of snapshots. In this section, the variables used to construct the reduced-order model are systematically selected based on the governing equations associated with the various components within the circuit. In the following sections, the selection of snapshots and establishment of the ROM for different components are introduced. To simplify the subsequent construction of the residual function and compute the coefficient matrix of the POD bases, the functions differentiated within the governing equations are chosen as the variables.

2.2.3 Core

Table 1 lists the selected variables contained in the snapshots, POD bases, and boundary conditions for the reactor core, which are determined from the single-channel thermal-hydraulic equations (1)–(3) and their discretization. The core variables can be reconstructed using the POD bases according to

$$\begin{cases} \phi &= \sum_{m=1}^{N_{p,c}} c_{m,c} P_{c,\phi,m}, \\ \phi &= \{\rho u, \rho uu, P, \mu u, \rho, \rho uh, Pu, \lambda T\}, \end{cases} \tag{43}$$

where $c_{m,c}$ is the coefficient corresponding to the core POD basis, and $N_{p,c}$ represents the core POD order.

For each internal node, by applying Eq. (43) into Eqs. (24), (26), and (28) and calculating the summation of the residue over all internal nodes, the accumulated residual functions of the core are generated as Eqs. (45), (49), and (46), where superscripts 'con,' 'mom,' and 'ene' represent the continuity, momentum, and energy, respectively, and NX_c represents the number of discretized grid points in the reactor core.

Similarly, to satisfy the inlet and outlet boundaries of the eight selected variables, the following two residual functions for the inlet and outlet are defined in Eqs. (47) and (48), respectively. Then, the total residual function of the core can be written as

$$E_c = E_c^{con} + E_c^{mom} + E_c^{ene} + E_c^{b,in} + E_c^{b,out}. \tag{44}$$

Subsequently, the coefficients c_m can be determined using the LSM to minimize the residual function E_c. With the determined c_m, the variables in Table 1 can be reconstructed using the POD bases, according to Eq. (43). The temperature, velocity, and pressure fields at each grid point of the

Table 1 Core variables, POD bases, and corresponding boundary conditions

Core variables	POD basis	Inlet boundary conditions	Outlet boundary conditions
ρu	$P_{c,\rho u}$	$\rho_{0,c} u_{0,c}$	–
ρuu	$P_{c,\rho uu}$	$\rho_{0,c} u_{0,c} u_{0,c}$	–
p	$P_{c,p}$	$p_{0,c}$	$dp/dx = 0$
μu	$P_{c,\mu u}$	$\mu_{0,c} u_{0,c}$	$\mu \cdot du/dx = 0$
ρ	$P_{c,\rho}$	$\rho_{0,c}$	–
ρuh	$P_{c,\rho uh}$	$\rho_{0,c} u_{0,c} h_{0,c}$	–
pu	$P_{c,pu}$	$p_{0,c} u_{0,c}$	–
λT	$P_{c,\lambda T}$	$\lambda_{0,c} T_{0,c}$	$\lambda \cdot dT/dx = 0$

core can be reconstructed based on the IF97 thermophysical properties.

$$E_{\mathrm{c}}^{\mathrm{con}} = \sum_{i=2}^{NX_{\mathrm{c}}} \left[\sum_{m=1}^{N_{p,\mathrm{c}}} c_{m,\mathrm{c}} \left(\frac{P_{\mathrm{c},\rho u,i,m} - P_{\mathrm{c},\rho u,i-1,m}}{\Delta x_{\mathrm{c}}} \right) \right]^2, \tag{45}$$

$$\begin{aligned} E_{\mathrm{c}}^{\mathrm{ene}} = \sum_{i=2}^{NX_{\mathrm{c}}-1} \Bigg[& \sum_{m=1}^{N_{p,\mathrm{c}}} c_{m,\mathrm{c}} \left(\frac{P_{\mathrm{c},\rho uh,i,m} - P_{\mathrm{c},\rho uh,i-1,m}}{\Delta x_{\mathrm{c}}} \right) \\ & + \sum_{m=1}^{N_{p,\mathrm{c}}} c_{m,\mathrm{c}} \left(\frac{P_{\mathrm{c},pu,i,m} - P_{\mathrm{c},pu,i-1,m}}{\Delta x_{\mathrm{c}}} \right) \\ & - \frac{1}{\Delta x_{\mathrm{c}}} \sum_{m=1}^{N_{p,\mathrm{c}}} c_{m,\mathrm{c}} \left(\frac{P_{\mathrm{c},\lambda T,i+1,m}}{\Delta x_{\mathrm{c}}} - 2\frac{P_{\mathrm{c},\lambda T,i,m}}{\Delta x_{\mathrm{c}}} + \frac{P_{\mathrm{c},\lambda T,i-1,m}}{\Delta x_{\mathrm{c}}} \right) - q_{\mathrm{c},i} \Bigg]^2, \end{aligned} \tag{46}$$

2.2.4 Steam generator

The variable selections based on the steam generator (SG) governing equations are shown in Table 2. Because the temperature at the last grid point of the parallel flow section is transferred to the last grid point of the counter-flow section, the inlet boundary condition for the coolant flow on the primary side is set as $T_{1,\mathrm{f},1} = T_{1,0}$. The outlet boundary condition of the coolant flow on the primary side is considered to be a fully developed boundary, indicating a temperature gradient of zero at the outlet of the counter-flow section.

Similar to Eq. (43), the SG variables can be reconstructed using the POD bases according to

$$\begin{aligned} E_{\mathrm{c}}^{\mathrm{b,in}} = & \left(\sum_{m=1}^{N_{p,\mathrm{c}}} c_{m,\mathrm{c}} P_{\mathrm{c},\rho u,1,m} - \rho_{0,\mathrm{c}} u_{0,\mathrm{c}} \right)^2 + \left(\sum_{m=1}^{N_{p,\mathrm{c}}} c_{m,\mathrm{c}} P_{\mathrm{c},\rho uu,1,m} - \rho_{0,\mathrm{c}} u_{0,\mathrm{c}} u_{0,\mathrm{c}} \right)^2 + \left(\sum_{m=1}^{N_{p,\mathrm{c}}} c_{m,\mathrm{c}} P_{\mathrm{c},p,1,m} - p_{0,\mathrm{c}} \right)^2 \\ & + \left(\sum_{m=1}^{N_{p,\mathrm{c}}} c_{m,\mathrm{c}} P_{\mathrm{c},\mu u,1,m} - \mu_{0,\mathrm{c}} u_{0,\mathrm{c}} \right)^2 + \left(\sum_{m=1}^{N_{p,\mathrm{c}}} c_{m,\mathrm{c}} P_{\mathrm{c},\rho,1,m} - \rho_{0,\mathrm{c}} \right)^2 + \left(\sum_{m=1}^{N_{p,\mathrm{c}}} c_{m,\mathrm{c}} P_{\mathrm{c},\rho uh,1,m} - \rho_{0,\mathrm{c}} u_{0,\mathrm{c}} h_{0,\mathrm{c}} \right)^2 \\ & + \left(\sum_{m=1}^{N_{p,\mathrm{c}}} c_{m,\mathrm{c}} P_{\mathrm{c},pu,1,m} - p_{0,\mathrm{c}} u_{0,\mathrm{c}} \right)^2 + \left(\sum_{m=1}^{N_{p,\mathrm{c}}} c_{m,\mathrm{c}} P_{\mathrm{c},\lambda T,1,m} - \lambda_{0,\mathrm{c}} T_{0,\mathrm{c}} \right)^2, \end{aligned} \tag{47}$$

$$\begin{aligned} E_{\mathrm{c}}^{\mathrm{b,out}} = & \Bigg[\sum_{m=1}^{N_{p,\mathrm{c}}} c_{m,\mathrm{c}} \left(\frac{P_{\mathrm{c},\rho uu,NX_{\mathrm{c}},m} - P_{\mathrm{c},\rho uu,NX_{\mathrm{c}}-1,m}}{\Delta x_{\mathrm{c}}} \right) + \frac{1}{\Delta x_{\mathrm{c}}} \sum_{m=1}^{N_{p,\mathrm{c}}} c_{m,\mathrm{c}} \left(\frac{P_{\mathrm{c},p,NX_{\mathrm{c}},m} - P_{\mathrm{c},p,NX_{\mathrm{c}}-1,m}}{\Delta x_{\mathrm{c}}} \right) \\ & + \sum_{m=1}^{N_{p,\mathrm{c}}} c_{m,\mathrm{c}} \left(\frac{P_{\mathrm{c},\mu u,NX_{\mathrm{c}},m} - P_{\mathrm{c},\mu u,NX_{\mathrm{c}}-1,m}}{\Delta x_{\mathrm{c}}} \right) + \frac{1}{2} \left(\frac{f}{D} + \frac{K_{\mathrm{sp}}}{\Delta x_{\mathrm{c}}} \right) \sum_{m=1}^{N_{p,\mathrm{c}}} c_{m,\mathrm{c}} P_{\mathrm{c},\rho uu,NX_{\mathrm{c}},m} + g \sum_{m=1}^{N_{p,\mathrm{c}}} c_{m,\mathrm{c}} P_{\mathrm{c},\rho,NX_{\mathrm{c}},m} \Bigg]^2 \\ & + \Bigg[\sum_{m=1}^{N_{p,\mathrm{c}}} c_{m,\mathrm{c}} \left(\frac{P_{\mathrm{c},\rho uh,NX_{\mathrm{c}},m} - P_{\mathrm{c},\rho uh,NX_{\mathrm{c}}-1,m}}{\Delta x_{\mathrm{c}}} \right) + \sum_{m=1}^{N_{p,\mathrm{c}}} c_{m,\mathrm{c}} \left(\frac{P_{\mathrm{c},pu,NX_{\mathrm{c}},m} - P_{\mathrm{c},pu,NX_{\mathrm{c}}-1,m}}{\Delta x_{\mathrm{c}}} \right) \\ & + \sum_{m=1}^{N_{p,\mathrm{c}}} c_{m,\mathrm{c}} \left(\frac{P_{\mathrm{c},\lambda T,NX_{\mathrm{c}},m} - P_{\mathrm{c},\lambda T,NX_{\mathrm{c}}-1,m}}{\Delta x_{\mathrm{c}}^2} \right) - q_{NX_{\mathrm{c}}} \Bigg]^2, \end{aligned} \tag{48}$$

$$\begin{aligned} E_{\mathrm{c}}^{\mathrm{mom}} = \sum_{i=2}^{NX_{\mathrm{c}}-1} \Bigg[& \sum_{m=1}^{N_{p,\mathrm{c}}} c_{m,\mathrm{c}} \left(\frac{P_{\mathrm{c},\rho uu,i,m} - P_{\mathrm{c},\rho uu,i-1,m}}{\Delta x_{\mathrm{c}}} \right) + \sum_{m=1}^{N_{p,\mathrm{c}}} c_{m,\mathrm{c}} \left(\frac{P_{\mathrm{c},p,i,m} - P_{\mathrm{c},p,i-1,m}}{\Delta x_{\mathrm{c}}} \right) \\ & - \sum_{m=1}^{N_{p,\mathrm{c}}} c_{m,\mathrm{c}} \left(\frac{P_{\mathrm{c},\mu u,i+1,m}}{\Delta x_{\mathrm{c}}^2} - 2\frac{P_{\mathrm{c},\mu u,i,m}}{\Delta x_{\mathrm{c}}^2} + \frac{P_{\mathrm{c},\mu u,i-1,m}}{\Delta x_{\mathrm{c}}^2} \right) + \frac{1}{2} \left(\frac{f}{D} + \frac{K_{\mathrm{sp}}}{\Delta x_{\mathrm{c}}} \right) \sum_{m=1}^{N_{p,\mathrm{c}}} c_{m,\mathrm{c}} P_{\mathrm{c},\rho uu,i,m} + g \sum_{m=1}^{N_{p,\mathrm{c}}} c_{m,\mathrm{c}} P_{\mathrm{c},\rho,i,m} \Bigg]^2. \end{aligned} \tag{49}$$

$$\phi = \sum_{m=1}^{N_{p,\mathrm{SG}}} c_{m,\mathrm{SG}} P_{\mathrm{SG},\phi,m},$$
$$\phi = \begin{cases} T_{1,\mathrm{f}}, T_{1,\mathrm{ad}}, T_{\mathrm{w,in,f}}, T_{\mathrm{w,out,f}}, T_{\mathrm{w,in,ad}}, T_{\mathrm{w,out,ad}}, \\ T_{2,\mathrm{r}}, \dfrac{T_{\mathrm{w,in,f}} - T_{1,\mathrm{f}}}{\rho_1 c_{\mathrm{p,f}}}, \dfrac{T_{\mathrm{w,in,ad}} - T_{1,\mathrm{ad}}}{\rho_1 c_{\mathrm{p,ad}}}, h_{\mathrm{s}}, \\ \dfrac{T_{\mathrm{w,out,f}} - T_{\mathrm{w,out,ad}} - 2T_{2,\mathrm{r}}}{c_{\mathrm{p},2}}, \end{cases} \tag{50}$$

where $c_{m,\mathrm{SG}}$ is the coefficient corresponding to the SG POD basis, and $N_{p,\mathrm{SG}}$ represents the POD order of the SG.

Let the number of discrete meshes in the parallel flow and counter-flow sections of the SG U-tube be defined as NX_{SG}. The dividing point between the preheating and boiling sections on the secondary side is positioned at grid location X_{SG}. Based on the discretized equations for the flow and wall heat transfer on the primary side, Eqs.(29) and (30), and applying Eq. (50), the residual function corresponding to these two equations can be formulated as follows, where superscript 1 represents the primary side:

$$\begin{cases} E_{\mathrm{SG}}^{\mathrm{primary}} = \sum_{i=2}^{NX_{\mathrm{SG}}} \left(\frac{m_1}{M_1 \Delta x_{\mathrm{SG}}} A_1 - \frac{4K_1}{M_1 d_{\mathrm{in}}} A_2 \right)^2 \\ \quad + \sum_{i=1}^{NX_{\mathrm{SG}}-1} \left(\frac{m_1}{M_1 \Delta x_{\mathrm{SG}}} A_3 + \frac{4K_1}{M_1 d_{\mathrm{in}}} A_4 \right)^2. \\ A_1 = \sum_{m=1}^{N_{p,\mathrm{SG}}} c_{m,\mathrm{SG}} \left(P_{\mathrm{SG},T_{1,\mathrm{f}},i,m} - P_{\mathrm{SG},T_{1,\mathrm{f}},i-1,m} \right) \\ A_2 = \sum_{m=1}^{N_{p,\mathrm{SG}}} c_{m,\mathrm{SG}} P_{\mathrm{SG,ta},i,m} \\ A_3 = \sum_{m=1}^{N_{p,\mathrm{SG}}} c_{m,\mathrm{SG}} \left(P_{\mathrm{SG},T_{1,\mathrm{ad}},i+1,m} - P_{\mathrm{SG},T_{1,\mathrm{ad}},i,m} \right) \\ A_4 = \sum_{m=1}^{N_{p,\mathrm{SG}}} c_{m,\mathrm{SG}} P_{\mathrm{SG,tb},i,m}. \end{cases} \tag{51}$$

Similarly, for the discretized equations representing the flow in the secondary side and the heat transfer on the outer surface of the U-tube, Eqs. (31) and (32), the residual function corresponding to these two equations can be formulated as follows, where superscript 2 represents the secondary side:

Table 2 Steam generator variables, POD bases, and corresponding boundary conditions

Core variables	POD basis	Inlet boundary conditions	Outlet boundary conditions
$T_{1,\mathrm{f}}$	$P_{\mathrm{SG},T_{1,\mathrm{f}}}$	$T_{1,0}$	–
$T_{1,\mathrm{ad}}$	$P_{\mathrm{SG},T_{1,\mathrm{ad}}}$	–	$\mathrm{d}T/\mathrm{d}x = 0$
$T_{\mathrm{w,in,f}}$	$P_{\mathrm{SG},T_{\mathrm{w,in,f}}}$	–	–
$T_{\mathrm{w,out,f}}$	$P_{\mathrm{SG},T_{\mathrm{w,out,f}}}$	–	–
$T_{\mathrm{w,in,ad}}$	$P_{\mathrm{SG},T_{\mathrm{w,in,ad}}}$	–	–
$T_{\mathrm{w,out,ad}}$	$P_{\mathrm{SG},T_{\mathrm{w,out,ad}}}$	–	–
$T_{2,\mathrm{r}}$	$P_{\mathrm{SG},T_{2,\mathrm{r}}}$	$T_{2,0}$	$\mathrm{d}T/\mathrm{d}x = 0$
$(T_{\mathrm{w,in,f}} - T_{1,\mathrm{f}})/(\rho_1 \cdot c_{\mathrm{p,f}})$	$P_{\mathrm{SG,ta}}$	–	–
$(T_{\mathrm{w,in,ad}} - T_{1,\mathrm{ad}})/(\rho_1 \cdot c_{\mathrm{p,ad}})$	$P_{\mathrm{SG,tb}}$	–	–
h_{s}	$P_{\mathrm{SG},h_{\mathrm{s}}}$	–	–
$(T_{\mathrm{w,out,f}} + T_{\mathrm{w,out,ad}} - 2T_{2,\mathrm{r}})/(c_{\mathrm{p},2})$	$P_{\mathrm{SG,tc}}$	–	–

$$\begin{cases} E_{\mathrm{SG}}^{\mathrm{secondary}} = \sum_{i=2}^{X_{\mathrm{SG}}} \left(\frac{m_2}{M_2 \Delta x_{\mathrm{SG}}} A_1 - \frac{nK_2 \pi d_{\mathrm{out}}}{M_2} A_2 \right)^2 \\ \quad + \sum_{i=X_{\mathrm{SG}}+1}^{NX_{\mathrm{SG}}} \left(\frac{m_2}{M_2 \Delta x_{\mathrm{SG}}} A_3 - \frac{nK_{2,\mathrm{s}} \pi d_{\mathrm{out}}}{M_2} A_4 \right)^2 \\ A_1 = \sum_{m=1}^{N_{p,\mathrm{SG}}} c_{m,\mathrm{SG}} \left(P_{\mathrm{SG},T_{2,\mathrm{r}},i,m} - P_{\mathrm{SG},T_{2,\mathrm{r}},i-1,m} \right) \\ A_2 = \sum_{m=1}^{N_{p,\mathrm{SG}}} c_{m,\mathrm{SG}} P_{\mathrm{SG,tc},i,m} \\ A_3 = \sum_{m=1}^{N_{p,\mathrm{SG}}} c_{m,\mathrm{SG}} \left(P_{\mathrm{SG},h_{\mathrm{s}},i,m} - P_{\mathrm{SG},h_{\mathrm{s}},i-1,m} \right) \\ A_4 = \sum_{m=1}^{N_{p,\mathrm{SG}}} c_{m,\mathrm{SG}} \left(P_{\mathrm{SG},T_{\mathrm{w,out,f}},i,m} \right. \\ \quad \left. + P_{\mathrm{SG},T_{\mathrm{w,out,ad}},i,m} - T_{2,\mathrm{s}} \right). \end{cases} \tag{52}$$

Based on the heat-balance equations for the U-tube inner wall, Eqs. (14) and (15), the corresponding residual function can be expressed as follows:

$$\begin{cases} E_{\mathrm{SG}}^{\mathrm{w,in}} = \sum_{i=1}^{NX_{\mathrm{SG}}} \left(\frac{2n\pi\lambda_{\mathrm{w}}}{M_{\mathrm{w}} c_{\mathrm{p,w}} \ln\left(\frac{d_{\mathrm{out}}}{d_{\mathrm{in}}}\right)} A_1 + \frac{nK_1 \pi d_{\mathrm{in}}}{M_{\mathrm{w}} c_{\mathrm{p,w}}} A_2 \right)^2 \\ \quad + \sum_{i=1}^{NX_{\mathrm{SG}}} \left(\frac{2n\pi\lambda_{\mathrm{w}}}{M_{\mathrm{w}} c_{\mathrm{p,w}} \ln\left(\frac{d_{\mathrm{out}}}{d_{\mathrm{in}}}\right)} A_3 + \frac{nK_1 \pi d_{\mathrm{in}}}{M_{\mathrm{w}} cp,w} A_4 \right)^2 \\ A_1 = \sum_{m=1}^{N_{p,\mathrm{SG}}} c_{m,\mathrm{SG}} (P_{\mathrm{SG},T_{\mathrm{w,out,f}},i,m} \\ \quad - P_{\mathrm{SG},T_{\mathrm{w,in,f}},i,m}) \\ A_2 = \sum_{m=1}^{N_{p,\mathrm{SG}}} c_{m,\mathrm{SG}} (P_{\mathrm{SG},T_{1,\mathrm{f}},i,m} \\ \quad - P_{\mathrm{SG},T_{\mathrm{w,in,f}},i,m}) \\ A_3 = \sum_{m=1}^{N_{p,\mathrm{SG}}} c_{m,\mathrm{SG}} (P_{\mathrm{SG},T_{\mathrm{w,out,ad}},i,m} \\ \quad - P_{\mathrm{SG},T_{\mathrm{w,in,ad}},i,m}) \\ A_4 = \sum_{m=1}^{N_{p,\mathrm{SG}}} c_{m,\mathrm{SG}} (P_{\mathrm{SG},T_{\mathrm{w,out,ad}},i,m} \\ \quad - P_{\mathrm{SG},T_{\mathrm{w,in,ad}},i,m}) \end{cases} \tag{53}$$

$$E_{\mathrm{SG}}^{\mathrm{b}} = \left[\sum_{m=1}^{N_{p,\mathrm{SG}}} c_{m,\mathrm{SG}} P_{\mathrm{SG},T_{1,\mathrm{f}},1,m} - T_{1,0} \right]^2 + \left[\sum_{m=1}^{N_{p,\mathrm{SG}}} c_{m,\mathrm{SG}} P_{\mathrm{SG},T_{2,\mathrm{r}},1,m} - T_{2,0} \right]^2 + \left[\sum_{m=1}^{N_{p,\mathrm{SG}}} c_{m,\mathrm{SG}} P_{\mathrm{SG},T_{1,\mathrm{f}},NX_{\mathrm{SG}},m} - \sum_{m=1}^{N_{p,\mathrm{SG}}} c_{m,\mathrm{SG}} P_{\mathrm{SG},T_{1,\mathrm{ad}},NX_{\mathrm{SG}},m} \right]^2 \tag{54}$$

Based on the heat transfer equations, Eqs. (16) and (17), the corresponding residual function can be expressed as follows:

$$\begin{cases} E_{\mathrm{SG}}^{\mathrm{w,out,parallel}} \\ \quad = \sum_{i=1}^{X_{\mathrm{SG}}} \left(\frac{2n\pi\lambda_{\mathrm{w}}}{M_{\mathrm{w}} c_{\mathrm{p,w}} \ln(d_{\mathrm{out}}/d_{\mathrm{in}})} A_1 + \frac{nK_2\pi d_{\mathrm{out}}}{M_{\mathrm{w}} c_{\mathrm{p,w}}} A_2 \right)^2 \\ \quad + \sum_{i=X_{\mathrm{SG}}+1}^{NX_{\mathrm{SG}}} \left(\frac{2n\pi\lambda_{\mathrm{w}}}{M_{\mathrm{w}} c_{\mathrm{p,w}} \ln(d_{\mathrm{out}}/d_{\mathrm{in}})} A_3 \right. \\ \quad \left. + \frac{nK_{2,s}\pi d_{\mathrm{out}}}{M_{\mathrm{w}} c_{\mathrm{p,w}}} \left(T_{2,s} - A_4 \right) \right)^2 . \\ A_1 = \sum_{m=1}^{N_{p,\mathrm{SG}}} c_{m,\mathrm{SG}} (P_{\mathrm{SG},T_{\mathrm{w,in,f}},i,m} \\ \qquad - P_{\mathrm{SG},T_{\mathrm{w,out,f}},i,m}) \\ A_2 = \sum_{m=1}^{N_{p,\mathrm{SG}}} c_{m,\mathrm{SG}} (P_{\mathrm{SG},T_{2,\mathrm{r}},i,m} \\ \qquad - P_{\mathrm{SG},T_{\mathrm{w,out,f}},i,m}) \\ A_3 = \sum_{m=1}^{N_{p,\mathrm{SG}}} c_{m,\mathrm{SG}} (P_{\mathrm{SG},T_{\mathrm{w,in,f}},i,m} \\ \qquad - P_{\mathrm{SG},T_{\mathrm{w,out,f}},i,m}) \\ A_4 = \sum_{m=1}^{N_{p,\mathrm{SG}}} c_{m,\mathrm{SG}} P_{\mathrm{SG},T_{\mathrm{w,out,f}},i,m}. \end{cases} \tag{55}$$

Based on the heat transfer equations, Eqs. (18) and (19), we can express the corresponding residual function using Eq. (56):

$$\begin{cases} E_{\mathrm{SG}}^{\mathrm{w,out,counter}} \\ \qquad = \sum_{i=1}^{X_{\mathrm{SG}}} \left[\frac{2n\pi\lambda_{\mathrm{w}}}{M_{\mathrm{w}} c_{\mathrm{p,w}} \ln(d_{\mathrm{out}}/d_{\mathrm{in}})} A_1 \right. \\ \qquad \left. + \frac{nK_2\pi d_{\mathrm{out}}}{M_{\mathrm{w}} c_{\mathrm{p,w}}} A_2 \right]^2 + \\ \qquad \sum_{i=X_{\mathrm{SG}}+1}^{NX_{\mathrm{SG}}} \left[\frac{2n\pi\lambda_{\mathrm{w}}}{M_{\mathrm{w}} c_{\mathrm{p,w}} \ln(d_{\mathrm{out}}/d_{\mathrm{in}})} A_3 \right. \\ \qquad \left. + \frac{nK_{2,s}\pi d_{\mathrm{out}}}{M_{\mathrm{w}} c_{\mathrm{p,w}}} \left(T_{2,\mathrm{s}} - A_4 \right) \right]^2 \\ A_1 = \sum_{m=1}^{N_{p,\mathrm{SG}}} c_{m,\mathrm{SG}} \left(P_{\mathrm{SG},T_{\mathrm{w,in,ad}},i,m} - P_{\mathrm{SG},T_{\mathrm{w,out,ad}},i,m} \right) \\ A_2 = \sum_{m=1}^{N_{p,\mathrm{SG}}} c_{m,\mathrm{SG}} \left(P_{\mathrm{SG},T_{\mathrm{w,in,ad}},i,m} - P_{\mathrm{SG},T_{\mathrm{w,out,ad}},i,m} \right) \\ A_3 = \sum_{m=1}^{N_{p,\mathrm{SG}}} c_{m,\mathrm{SG}} \left(P_{\mathrm{SG},T_{\mathrm{w,in,ad}},i,m} - P_{\mathrm{SG},T_{\mathrm{w,out,ad}},i,m} \right) \\ A_4 = \sum_{m=1}^{N_{p,\mathrm{SG}}} c_{m,\mathrm{SG}} P_{\mathrm{SG},T_{\mathrm{w,out,ad}},i,m} \end{cases} . \tag{56}$$

The residual functions corresponding to the inlet boundary conditions of the coolant on both the primary and secondary sides, as well as the outlet of the parallel flow and inlet of the counter-flow on the primary side, can be expressed by Eq. (54). The overall residual function E_{SG} is as follows:

$$\begin{aligned} E_{\mathrm{SG}} = E_{\mathrm{SG}}^{\mathrm{primary}} + E_{\mathrm{SG}}^{\mathrm{secondary}} + E_{\mathrm{SG}}^{\mathrm{w,in}} \\ + E_{\mathrm{SG}}^{\mathrm{w,out,parallel}} + E_{\mathrm{SG}}^{\mathrm{w,out,counter}} + E_{\mathrm{SG}}^{\mathrm{b}}. \end{aligned} \tag{57}$$

Subsequently, the coefficients $c_{m,\mathrm{SG}}$ are determined using the LSM, and the temperature distribution inside the SG is reconstructed based on Eq. (50).

Table 3 Pipe variables, POD bases, and corresponding boundary conditions

Core variables	POD basis	Inlet boundary conditions	Outlet boundary conditions
ρu	$P_{\mathrm{p},\rho u}$	$\rho_{0,\mathrm{p}} u_{0,\mathrm{p}}$	–
ρuu	$P_{\mathrm{p},\rho uu}$	$\rho_{0,\mathrm{p}} u_{0,\mathrm{p}} u_{0,\mathrm{p}}$	–
p	$P_{\mathrm{p},p}$	$p_{0,\mathrm{p}}$	$\mathrm{d}p/\mathrm{d}x = 0$
μu	$P_{\mathrm{p},\mu u}$	$\mu_{0,\mathrm{p}} u_{0,\mathrm{p}}$	$\mu \cdot \mathrm{d}u/\mathrm{d}x = 0$
ρ	$P_{\mathrm{p},\rho}$	$\rho_{0,\mathrm{p}}$	–
ρuh^*	$P_{\mathrm{p},\rho uh}$	$\rho_{0,\mathrm{p}} u_{0,\mathrm{p}} h_{0,\mathrm{p}}$	–
λT^*	$P_{\mathrm{p},\lambda T}$	$\lambda_{0,\mathrm{p}} T_{0,\mathrm{p}}$	$\lambda \cdot \mathrm{d}T/\mathrm{d}x = 0$

*ρuh^* and λT^* are only used in heat transfer pipes

2.2.5 Pipes

The selected variables and boundary conditions for the pipes are presented in Table 3. The thermal-hydraulic variables of the pipe can be reconstructed using the following equation:

$$\begin{aligned} &\phi = \sum_{m}^{N_{p,\mathrm{p}}} c_{m,\mathrm{p}} P_{\mathrm{p},\phi,m}, \\ &\phi \in \{\rho, \rho u, \rho uu, p, \mu u, \rho uh^*, \lambda T^*\}, \end{aligned} \tag{58}$$

where $c_{m,\mathrm{p}}$ is the coefficient corresponding to the POD basis of the pipes, and $N_{p,\mathrm{p}}$ represents their POD order. Similar to the previous sections, the residual functions of the pipe for the continuity and momentum equations at the internal grids can be defined using Eqs. (59) and (60), respectively.

$$E_{\mathrm{p}}^{\mathrm{con}} = \sum_{i=2}^{NX_{\mathrm{p}}} \left[\sum_{m=1}^{N_{p,\mathrm{p}}} c_{m,\mathrm{p}} \left(\frac{P_{\mathrm{p},\rho u,i,m} - P_{\mathrm{p},\rho u,i-1,m}}{\Delta x_{\mathrm{p}}} \right) \right]^2, \tag{59}$$

$$\begin{aligned} E_{\mathrm{p}}^{\mathrm{mom}} = \sum_{i=2}^{NX_{\mathrm{p}}-1} \Bigg[&\sum_{m=1}^{N_{p,\mathrm{p}}} c_{m,\mathrm{p}} \left(\frac{P_{\mathrm{p},\rho uu,i,m} - P_{\mathrm{p},\rho uu,i-1,m}}{\Delta x_{\mathrm{p}}} \right) \\ &+ \sum_{m=1}^{N_{p,\mathrm{p}}} c_{m,\mathrm{p}} \left(\frac{P_{\mathrm{p},p,i,m} - P_{\mathrm{p},p,i-1,m}}{\Delta x_{\mathrm{p}}} \right) \\ &- \sum_{m=1}^{N_{p,\mathrm{p}}} c_{m,\mathrm{p}} \left(\frac{P_{\mathrm{p},\mu u,i+1,m} - 2P_{\mathrm{p},\mu u,i,m} + P_{\mathrm{p},\mu u,i-1,m}}{\Delta x_{\mathrm{p}}^2} \right) \\ &+ \frac{f}{2D} \sum_{m=1}^{N_{p,\mathrm{p}}} c_{m,\mathrm{p}} P_{\mathrm{p},\rho uu,i,m} + g \sin\theta \sum_{m=1}^{N_{p,\mathrm{p}}} c_{m,\mathrm{p}} P_{\mathrm{p},\rho,i,m} \Bigg]^2, \end{aligned} \tag{60}$$

where NX_{p} denotes the number of discretized grid points in the pipes.

$$E_{\mathrm{p}}^{\mathrm{b,in}} = \left(\sum_{m=1}^{N_{p,\mathrm{p}}} c_{m,\mathrm{p}} P_{\mathrm{p},\rho u,1,m} - \rho_{0,\mathrm{p}} u_{0,\mathrm{p}}\right)^2 + \left(\sum_{m=1}^{N_{p,\mathrm{p}}} c_{m,\mathrm{p}} P_{\mathrm{p},\rho uu,1,m} - \rho_{0,\mathrm{p}} u_{0,\mathrm{p}} u_{0,\mathrm{p}}\right)^2 + \left(\sum_{m=1}^{N_{p,\mathrm{p}}} c_{m,\mathrm{p}} P_{\mathrm{p},p,1,m} - p_{0,\mathrm{p}}\right)^2 + \left(\sum_{m=1}^{N_{p,\mathrm{p}}} c_{m,\mathrm{p}} P_{\mathrm{p},\mu u,1,m} - \mu_{0,\mathrm{p}} u_{0,\mathrm{p}}\right)^2 + \left(\sum_{m=1}^{N_{p,\mathrm{p}}} c_{m,\mathrm{p}} P_{\mathrm{p},\rho,1,m} - \rho_{0,\mathrm{p}}\right)^2. \tag{61}$$

Based on the boundary conditions listed in Table 3, the residual functions at the inlet boundary of the pressure drop pipes can be expressed using Eq. (61).

The governing equations for the outlet boundary grids of the pressure drop pipes can be discretized as follows:

$$\frac{(\rho uu)_{\mathrm{p},NX_\mathrm{p}} - (\rho uu)_{\mathrm{p},NX_\mathrm{p}-1}}{\Delta x_\mathrm{p}} = \frac{1}{\Delta x_\mathrm{p}}\left(-\frac{(\mu u)_{\mathrm{p},NX_\mathrm{p}} - (\mu u)_{\mathrm{p},NX_\mathrm{p}-1}}{\Delta x_\mathrm{p}}\right) - \frac{P_{\mathrm{p},NX_\mathrm{p}} - P_{\mathrm{p},NX_\mathrm{p}-1}}{\Delta x_\mathrm{p}} - \frac{f}{2D}\rho_{\mathrm{p},NX_\mathrm{p}} u^2_{\mathrm{p},NX_\mathrm{p}} - \rho_{\mathrm{p},NX_\mathrm{p}} g \sin\theta. \tag{62}$$

The residual function based on the expression above can be represented as follows:

$$E_{\mathrm{p}}^{\mathrm{b,out}} = \left[\sum_{m=1}^{N_{p,\mathrm{p}}} c_{m,\mathrm{p}}\left(\frac{P_{\mathrm{p},\rho uu,NX_\mathrm{p},m} - P_{\mathrm{p},\rho uu,NX_\mathrm{p}-1,m}}{\Delta x_\mathrm{p}}\right) + \sum_{m=1}^{N_{p,\mathrm{p}}} c_{m,\mathrm{p}}\left(\frac{P_{\mathrm{p},p,NX_\mathrm{p},m} - P_{\mathrm{p},p,NX_\mathrm{p}-1,m}}{\Delta x_\mathrm{p}^2}\right) + \sum_{m=1}^{N_{p,\mathrm{p}}} c_{m,\mathrm{p}}\left(\frac{P_{\mathrm{p},\mu u,NX_\mathrm{p},m} - P_{\mathrm{p},\mu u,NX_\mathrm{p}-1,m}}{\Delta x_\mathrm{p}}\right) + \frac{f}{2D}\sum_{m=1}^{N_{p,\mathrm{p}}} c_{m,\mathrm{p}} P_{\mathrm{p},\rho uu,NX_\mathrm{p},m} + g\sin\theta \sum_{m=1}^{N_{p,\mathrm{p}}} c_{m,\mathrm{p}} P_{\mathrm{p},\rho,NX_\mathrm{p},m}\right]^2. \tag{63}$$

Then, the residual function of the pressure drop pipe can be written as

$$E_\mathrm{p} = E_\mathrm{p}^{\mathrm{con}} + E_\mathrm{p}^{\mathrm{mom}} + E_\mathrm{p}^{\mathrm{b,in}} + E_\mathrm{p}^{\mathrm{b,out}}. \tag{64}$$

For discretized heat-exchange pipes, the residual function includes an additional energy equation term compared to discretized pressure drop pipes. The residual function at the internal grid of the energy equation is expressed as follows:

$$E_\mathrm{p}^{\mathrm{ene}} = \sum_{i=2}^{NX_\mathrm{p}-1}\left[\sum_{m=1}^{N_{p,\mathrm{p}}} c_{m,\mathrm{p}}\left(\frac{P_{\mathrm{p},\rho uh,i,m} - P_{\mathrm{p},\rho uh,i-1,m}}{\Delta x_\mathrm{p}}\right) - \sum_{m=1}^{N_{p,\mathrm{p}}} c_{m,\mathrm{p}} \frac{P_{\mathrm{p},\lambda T,i+1,m} - 2P_{\mathrm{p},\lambda T,i,m} + P_{\mathrm{p},\lambda T,i-1,m}}{\Delta x_\mathrm{p}^2} - q_{\mathrm{p},i}\right]^2. \tag{65}$$

The residual function at the inlet grid of the energy equation is expressed as follows:

$$E_\mathrm{p}^{\mathrm{ene,in}} = \left(\sum_{m=1}^{N_{p,\mathrm{p}}} c_{m,\mathrm{p}} P_{\mathrm{p},\rho uh,1,m} - \rho_{0,\mathrm{p}} u_{0,\mathrm{p}} h_{0,\mathrm{p}}\right)^2 + \left(\sum_{m=1}^{N_{p,\mathrm{p}}} c_{m,\mathrm{p}} P_{\mathrm{p},\lambda T,1,m} - \lambda_{0,\mathrm{p}} T_{0,\mathrm{p}}\right)^2. \tag{66}$$

The discretized form of the energy equation at the outlet grid can be written as

$$\frac{(\rho uh)_{\mathrm{p},NX_\mathrm{p}} - (\rho uh)_{\mathrm{p},NX_\mathrm{p}-1}}{\Delta x_\mathrm{p}} = q_{\mathrm{p},NX_\mathrm{p}} + \frac{1}{\Delta x_\mathrm{p}}\left(-\frac{(\lambda T)_{\mathrm{p},NX_\mathrm{p}} - (\lambda T)_{\mathrm{p},NX_\mathrm{p}-1}}{\Delta x_\mathrm{p}}\right). \tag{67}$$

The corresponding residual function is expressed as follows:

$$E_\mathrm{p}^{\mathrm{ene,out}} = \left[\sum_{m=1}^{NX_{p,\mathrm{p}}} c_{m,\mathrm{p}}\left(\frac{P_{\mathrm{p},\rho uh,NX_\mathrm{p},m} - P_{\mathrm{p},\rho uh,NX_\mathrm{p}-1,m}}{\Delta x_\mathrm{p}}\right) + \sum_{m=1}^{N_{p,\mathrm{p}}} c_{m,\mathrm{p}}\left(\frac{P_{\mathrm{p},\lambda T,NX_\mathrm{p},m} - P_{\mathrm{p},\lambda T,NX_\mathrm{p}-1,m}}{\Delta x_\mathrm{p}^2}\right) - q_{NX_\mathrm{p}}\right]^2. \tag{68}$$

Therefore, the residual function for the discretized heat-exchange pipes can be represented as

$$E_{\mathrm{H,p}} = E_\mathrm{p} + E_\mathrm{p}^{\mathrm{ene}} + E_\mathrm{p}^{\mathrm{ene,in}} + E_\mathrm{p}^{\mathrm{ene,out}}. \tag{69}$$

Table 4 POD order for different components

Component	N_p
Core	2
Heat pipe section 1	3
Heat pipe section 2	3
Steam generator	2
Pressure drop pipe	3
Cold pipe section	3

Table 5 Core design parameters and FOM simulation results

	Design value	Simulation value	Errors (%)
Inlet temperature (K)	552.59	552.554	0.006515
Outlet temperature (K)	597.81	597.306	0.084308
Average flow rate (m/s)	4.816	4.81658	0.012043
Core pressure drop (MPa)	0.43	0.43512	1.190698

Subsequently, the LSM is applied to solve the coefficients $c_{m,\mathrm{p}}$ for different pipes, and the required variables are reconstructed.

2.2.6 Implementation of ROMs

After establishing a reduced-order model for each component, the implementation of the proposed ROMs for predicting different working conditions is listed as follows:

Offline stage:

Step 1: The key state parameters for different equipment and circuit systems such as inlet flow rate, inlet temperature, and core power are determined.

Step 2: The ranges of different state parameters are determined based on the actual operating conditions, and a series of state points are selected within these ranges for a full-order simulation to obtain snapshots.

Step 3: The POD process is imposed according to Sect. 2.2.1 to obtain the POD bases, and a reduced-order model is built for the primary circuit.

Online stage:

Step 1: The state parameters are set for the state to be predicted.

Step 2: The POD coefficients c_m are calculated for each component using Eqs. (44), (57), (64), (69), and (42).

Step 3: The temperature, pressure, and velocity distributions of the unknown state are reconstructed using Eqs. (43), (50), and (58).

3 Results and discussion

This section presents a validation of the full-order model of the primary circuit system against the designated parameters. After validation, the results obtained from the reduced-order model corresponding to the primary circuit of the reactor are analyzed and compared. The reduced-order model is validated in two parts. First, the results of the reduced-order model are compared with those of the FOM corresponding to the operating conditions included in the snapshots. The second part uses the reduced-order model to calculate the unknown operating conditions not included in the snapshots and compares them with the full-order results. In this study, 11 specific operating conditions covering a 70–100% rating power are chosen as snapshots. Under different operating conditions, the core power and boundary conditions on the secondary side of the steam generator are considered as the input parameters. These selected snapshots serve as the foundation for generating POD bases and establishing the corresponding POD reduced-order models. Following Eq. (39), the values of N_p for each component of the primary circuit are listed in Table 4.

Table 6 SG design parameters and FOM simulation results

	Design value	Simulation value	Errors (%)
Primary side inlet temperature (K)	594.25	594.212	0.006395
Primary side outlet temperature (K)	553.75	553.664	0.01553

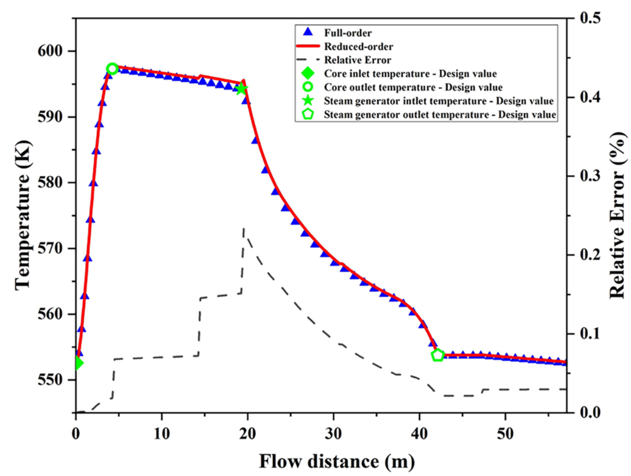

Fig. 7 (Color online) 100% operating condition temperature distribution

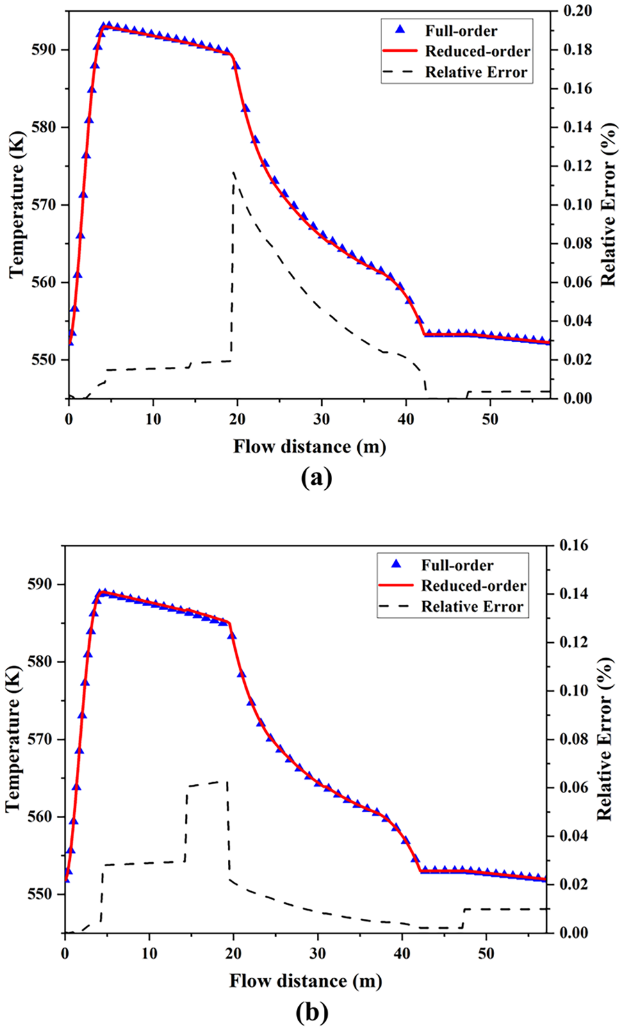

Fig. 8 Temperature distribution of **a** 86.5% core power and **b** 74.5% core power along the flow direction

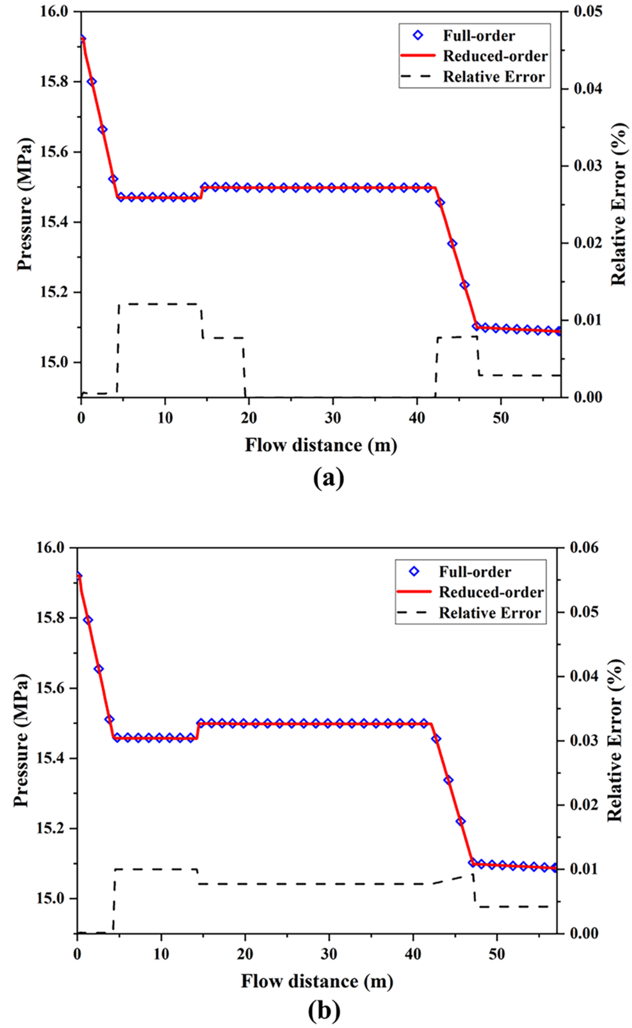

Fig. 9 Pressure distribution of **a** 86.5% core power and **b** 74.5% core power along the flow direction

3.1 Full-order model verification

First, the simulation results of the primary circuit FOM developed in this study are compared with the design parameters of the AP1000 reactor [37]. Tables 5 and 6 compare the full-power operating conditions with the full-order calculation results for the AP1000 reactor core and SG sections, respectively. These comparisons indicate that the proposed FOM can be used to accurately simulate the thermal-hydraulic behavior of the system circuit. For verification, snapshots are obtained using the proposed FOM.

3.2 Reduced-order model verification

Second, the full-power operating conditions of the snapshot set are used to verify the correctness of the reduced-order model. Figure 7 provides the temperature distribution of the reduced-order model and FOM, which is compared with those of the design values. This comparison shows that both the FOM and reduced-order model solutions are in good agreement with the design values. The reduced-order model accurately predicts the physical distribution of a circuit system.

Figure 7 also further provides the relative error between the reduced-order model and FOM solutions. The maximum relative error between the results of the reduced-order model and the FOM is 0.233% for the primary circuit of the entire reactor. Compared with the design parameters, the relative deviation of the core inlet temperature calculated by the reduced-order model is 0.147%, that of the core exit temperature is 0.018%, that of the SG inlet temperature is 0.145%, and that of the SG outlet temperature is 0.006%,

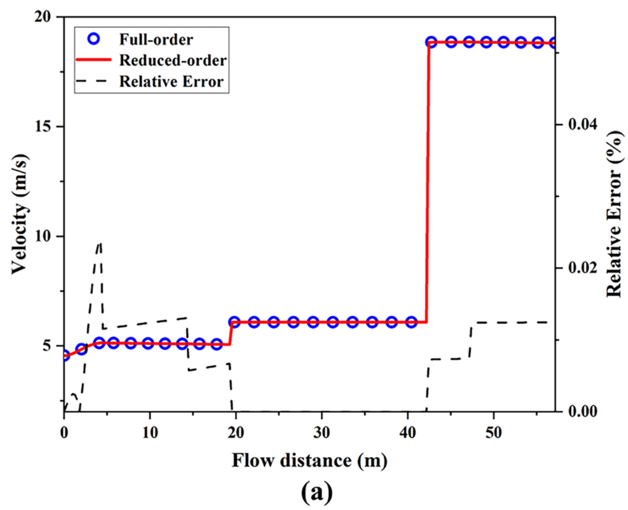

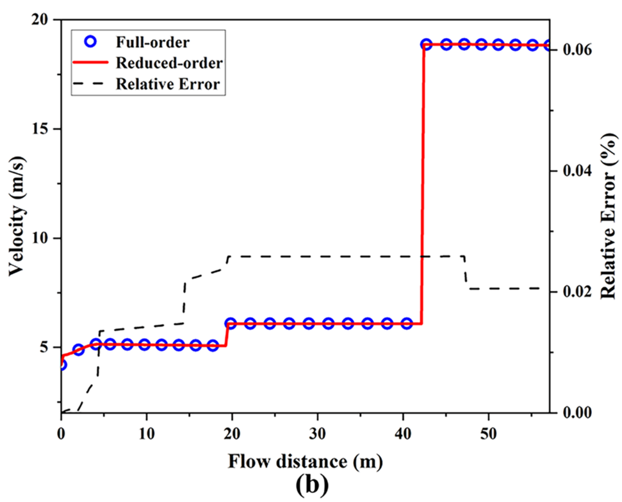

Fig. 10 Velocity distribution of **a** 86.5% core power and **b** 74.5% core power along the flow direction

indicating that the proposed reduced-order model can accurately predict the thermal-hydraulic behavior of the system circuit.

Under full-power operating conditions, the computational time for the FOM and reduced-order model is 63.9 s and 0.0404 s, respectively. The reduced-order model shows an acceleration ratio of 1582 times, indicating that the proposed reduced-order model can effectively improve the computing speed. The FOM computing time of our self-developed code is similar to those of other widely used programs with the same accuracy. This further indicates that the proposed reduced-order model can be used to effectively accelerate reactor circuit calculations. In digital twin applications, the efficiency of the current reduced-order models can strongly support real-time or even ultra-real-time assimilation simulations.

Finally, to verify the extensibility and accuracy of the reduced-order model, 86.5% and 74.5% power operating conditions, which are not included in the snapshots, are calculated using the reduced-order model. The temperature, pressure, and velocity fields obtained from the reduced-order model are compared with the FOM results. Under operating conditions of 74.5% and 86.5% power, the acceleration ratios of the reduced-order model are 1768 and 1493 times, respectively.

Figure 8 illustrates the temperature distribution along the flow direction calculated by both the full-order and reduced-order models under operating conditions of 86.5% and 74.5% power. In addition, the relative errors at various grid points are presented. The reduced-order results agreed well with the full-order results. For the 86.5% power operating condition, the maximum relative error is 0.117%, and the average error is 0.015%; for the 74.5% power operating condition, the maximum relative error is 0.063%, and the average error is 0.019%.

The pressure field distributions for both the 86.5% and 74.5% full-power operating conditions and the relative errors between the reduced- and full-order results are illustrated in Fig. 9. Under the 86.5% operating condition, the maximum relative error is 0.012%, and the average error is 0.006%; under the 74.5% operating condition, the maximum relative error is 0.01%, and the average error is 0.007%.

Figure 10 presents the velocity field distributions for both the 86.5% and 74.5% power operating conditions. The reduced-order results are in good agreement with the full-order results. Under the 86.5% operating condition, the maximum relative error is 0.024%, and the average error is 0.008%; under the 74.5% operating condition, the maximum relative error is 0.026%, and the average error is 0.02%. These solutions indicate that the proposed reduced-order model can accurately predict the physical processes of unknown states.

4 Conclusion

In this study, an RO-PTSC based on POD and LSM was developed. A full-order circuit model is used to generate snapshots under various operating conditions. The POD bases were subsequently constructed from the snapshots. Then, for all main circuit components, the residual functions were constructed based on their governing equations, and the POD coefficient matrices were calculated using the LSM. The variables of interest in the governing equations could be reconstructed using these coefficient matrices and the POD basis. Subsequently, the temperature, pressure, and velocity fields were obtained by employing the combinatorial relationships between the reconstructed variables and invoking the IF97 physical property calculation function. To verify the proposed RO-PTSC method, the AP1000 primary circuit was simulated using a reduced-order model and compared with the full-order results. For 86.5% and 74.5% power operating conditions, the temperature, pressure, and velocity fields along the flow direction from the reduced-order model agreed well with the full-order results and attained an acceleration ratio exceeding 1000.

Author contributions All authors contributed to the study conception and design. Material preparation, data collection, and analysis were performed by Z-LZ, Y-HW, Z-XL, H-HC, and YM. The first draft of the manuscript was written by Z-LZ and Y-HW, and all authors commented on previous versions of the manuscript. All authors read and approved the final manuscript.

Data availability The data that support the findings of this study are openly available in Science Data Bank at https://cstr.cn/31253.11.sciencedb.09167 and https://www.doi.org/10.57760/sciencedb.09167.

Declarations

Conflict of interest The authors declare that they have no conflict of interest.

References

1. W.W. Wang, G.H. Su, S.Z. Qiu et al., Thermal hydraulic phenomena related to small break LOCAs in AP1000. Prog. Nucl. Energy **53**, 407–419 (2011). https://doi.org/10.1016/j.pnucene.2011.02.007
2. H.Y. Gu, Y.Q. Yu, X. Cheng et al., Numerical analysis of thermal-hydraulic behavior of supercritical water in vertical upward/downward flow channels. Nucl. Sci. Tech. **19**, 178–186 (2008). https://doi.org/10.1016/j.pnucene.2011.02.007
3. D.L. Zhang, S.Z. Qiu, C.L. Liu et al., Steady thermal hydraulic analysis for a molten salt reactor. Nucl. Sci. Tech. **19**, 187–192 (2008). https://doi.org/10.1016/S1001-8042(08)60048-2
4. S.F. Huang, D.X. Gong, C. Li et al., Prediction of flow and temperature distributions in a high flux research reactor using the porous media approach. Sci. Technol. Nucl. Ins. **2017**, 7152730 (2017). https://doi.org/10.1155/2017/7152730
5. D.L. Zhang, S.Z. Qiu, G.H. Su, Development of a safety analysis code for molten salt reactors. Nucl. Eng. Des. **239**, 2778–2785 (2009). https://doi.org/10.1016/j.nucengdes.2009.08.020
6. D. Stork, P. Agostini, J.L. Boutard et al., Developing structural, high-heat flux and plasma facing materials for a near-term DEMO fusion power plant: the EU assessment. J. Nucl. Mater. **455**, 277–291 (2014). https://doi.org/10.1016/j.jnucmat.2014.06.014
7. C. Kloss, C. Goniva, A. Hager et al., Models, algorithms and validation for opensource DEM and CFD-DEM. Prog. Comput. Fluid Dyn. **12**, 140–152 (2012). https://doi.org/10.1504/pcfd.2012.047457
8. J.P. Cheng, L.M. Yan, F.C. Li, CFD simulation of a four-loop PWR at asymmetric operation conditions. Nucl. Eng. Des. **300**, 591–600 (2016). https://doi.org/10.1016/j.nucengdes.2016.02.018
9. C. Fiorina, D. Lathouwers, M. Aufiero et al., Modelling and analysis of the MSFR transient behaviour. Ann. Nucl. Energy **64**, 485–498 (2014). https://doi.org/10.1016/j.anucene.2013.08.003
10. J. Yang, X. Sui, Y.P. Huang et al., Assessment of reactor flow field prediction based on deep learning and model reduction. Ann. Nucl. Energy **179**, 109367 (2022). https://doi.org/10.1016/j.anucene.2022.109367
11. Z. Dong, Y.F. Pan, A lumped-parameter dynamical model of a nuclear heating reactor cogeneration plant. Energy **145**, 638–656 (2018). https://doi.org/10.1016/j.energy.2017.12.153
12. S. Sugawara, Y. Miyamoto, FIDAS: detailed subchannel analysis code based on the three-fluid and three-field model. Nucl. Eng. Des. **120**, 147–161 (1990). https://doi.org/10.1016/0029-5493(90)90369-9
13. J.C. Wang, Q. Wang, M. Ding, Review on neutronic/thermal-hydraulic coupling simulation methods for nuclear reactor analysis. Ann. Nucl. Energy **137**, 107165 (2020). https://doi.org/10.1016/j.anucene.2019.107165
14. J.W. Thomas, *Numerical Partial Differential Equations: Finite Difference Methods* (Springer, New York, 2013)
15. A.A. Karve, R. Uddin, J.J. Dorning, Stability analysis of BWR nuclear-coupled thermal-hydraulics using a simple model. Nucl. Eng. Des. **177**, 155–177 (1997). https://doi.org/10.1016/S0029-5493(97)00192-1
16. D. Bestion, The physical closure laws in the CATHARE code. Nucl. Eng. Des. **124**, 229–245 (1990). https://doi.org/10.1016/0029-5493(90)90294-8
17. A. Cammi, F. Casella, M.E. Ricotti et al., An object-oriented approach to simulation of IRIS dynamic response. Prog. Nucl. Energy **53**, 48–58 (2011). https://doi.org/10.1016/j.pnucene.2010.09.004
18. C. Fazekas, G. Szederkenyi, K.M. Hangos, A simple dynamic model of the primary circuit in VVER plants for controller design purposes. Nucl. Eng. Des. **237**, 1071–1087 (2007). https://doi.org/10.1016/j.nucengdes.2006.12.002
19. D.G. Cacuci, *Handbook of Nuclear Engineering* (Springer, New York, 2010)
20. M.S. Greenwood, B.R. Betzler, A.L. Qualls et al., Demonstration of the advanced dynamic system modeling tool TRANSFORM in a molten salt reactor application via a model of the molten salt demonstration reactor. Nucl. Technol. **206**, 478–504 (2020). https://doi.org/10.1080/00295450.2019.1627124
21. Y.H. Zheng, J. Lapins, E. Laurien et al., Thermal hydraulic analysis of a pebble-bed modular high temperature gas-cooled reactor with ATTICA3D and THERMIX codes. Nucl. Eng. Des. **246**, 286–297 (2012). https://doi.org/10.1016/j.nucengdes.2012.02.014
22. R.W. Moir, R.L. Bieri, X.M. Chen et al., HYLIFE-II: a molten-salt inertial fusion energy power plant design. Fusion Technol. **25**, 5–25 (1994). https://doi.org/10.13182/FST94-A30234
23. J. Bae, G. Kim, S.J. Lee, Real-time prediction of nuclear power plant parameter trends following operator actions. Expert Syst. Appl. **186**, 115848 (2021). https://doi.org/10.3390/en15186588
24. F. Bouttier, P. Courtier, Data assimilation concepts and methods March 1999. Meteorol. Train. Course Lect. Ser. ECMWF **718**, 59 (2002)
25. H.L. Gong, S.B. Cheng, Z. Chen et al., An efficient digital twin based on machine learning SVD autoencoder and generalised latent assimilation for nuclear reactor physics. Ann. Nucl. Energy **179**, 109431 (2022). https://doi.org/10.1016/j.anucene.2022.109431
26. D.J. Lucia, P.S. Beran, W.A. Silva, Reduced-order modeling: new approaches for computational physics. Prog. Aerosp. Sci. **40**, 51–117 (2004). https://doi.org/10.1016/j.paerosci.2003.12.001
27. Q.H. Yang, Y. Yang, Y.T. Deng et al., Physics-constrained neural network for solving discontinuous interface K-eigenvalue problem with application to reactor physics. Nucl. Sci. Tech. **34**, 161 (2023). https://doi.org/10.1007/s41365-023-01313-0
28. J.Q. Zeng, H.X. Zhang, H.L. Gong et al., Ensemble Bayesian method for parameter distribution inference: application to

reactor physics. Nucl. Sci. Tech. **34**, 199 (2023). https://doi.org/10.1007/s41365-023-01356-3

29. Y. Yang, H.L. Gong, Q.L. He et al., conducted an uncertainty analysis of a data-enabled physics-informed neural network to solve the neutron diffusion eigenvalue problem. Nucl. Sci. Eng. (2023). https://doi.org/10.1080/00295639.2023.2236840
30. M. Hutton, B. Friedland, Routh approximations for reducing order of linear, time-invariant systems. IEEE Trans. Automat. Contr. **20**, 329–337 (1975). https://doi.org/10.1109/TAC.1975.1100953
31. Z. Bai, Krylov subspace techniques for reduced-order modeling of large-scale dynamical systems. Appl. Numer. Math. **43**, 9–44 (2002). https://doi.org/10.1016/s0168-9274(02)00116-2
32. Y. Shamash, Linear system reduction using Pade approximation to allow retention of dominant modes. Int. J. Control **21**, 257–272 (1975). https://doi.org/10.1080/00207177508921985
33. G. Stabile, G. Rozza, Finite volume POD-Galerkin stabilised reduced order methods for the parametrised incompressible Navier–Stokes equations. Comput. Fluids **173**, 273–284 (2018). https://doi.org/10.1016/j.compfluid.2018.01.035
34. P.J. Schmid, Dynamic mode decomposition of numerical and experimental data. J. Fluid Mech. **656**, 5–28 (2010). https://doi.org/10.1017/S0022112010001217
35. A. Sartori, A. Cammi, L. Luzzi et al., A multi-physics reduced order model for the analysis of Lead Fast Reactor single channel. Ann. Nucl. Energy **87**, 198–208 (2016). https://doi.org/10.1016/j.anucene.2015.09.002
36. S. Chaturantabut, D.C. Sorensen, Nonlinear model reduction via discrete empirical interpolation. SIAM J. Sci. Comput. **32**, 2737–2764 (2010). https://doi.org/10.1137/090766498
37. T.L. Schulz, Westinghouse AP1000 advanced passive plant. Nucl. Eng. Des. **236**, 1547–1557 (2006). https://doi.org/10.1016/j.nucengdes.2006.03.049
38. B. Sutharshan, M. Mutyala, R.P. Vijuk et al., The AP1000™ reactor: passive safety and modular design. Energy Proced. **7**, 293–302 (2011). https://doi.org/10.1016/j.egypro.2011.06.038
39. R. Zhu, Y. Liu, X. Wang et al., The research on AP1000 nuclear main pumps' complete characteristics and the normalization method. Ann. Nucl. Energy **99**, 1–8 (2017). https://doi.org/10.1016/j.anucene.2016.08.014
40. J.W. Spore, B.S. Shiralkar, A generalized computational model for transient two phase thermal hydraulics in a single channel, in: International Heat Transfer Conference (1978)
41. M. Schikorr, E. Bubelis, L. Mansani et al., Proposal for pressure drop prediction for a fuel bundle with grid spacers using Rehme pressure drop correlations. Nucl. Eng. Des. **240**, 1830–1842 (2010). https://doi.org/10.1016/j.nucengdes.2010.03.039
42. S. Patankar, *Numerical Heat Transfer and Fluid Flow* (Taylor, Francis, London, 2018)
43. I.E. Idelchik, *Handbook of Hydraulic Resistance*, United States (1986)
44. G.L. Zhang, Y. Zhang, Y.L. Yang et al., Dynamic heat transfer performance study of steam generator based on distributed parameter method. Ann. Nucl. Energy **63**, 658–664 (2014). https://doi.org/10.1016/j.anucene.2013.09.005
45. D. Jo, O.S. Al-Yahia, A. Raga'im et al., Experimental investigation of convective heat transfer in a narrow rectangular channel for upward and downward flows. Nucl. Eng. Technol. **46**, 195–206 (2014). https://doi.org/10.5516/NET.02.2013.057
46. W.M. Rohsenow, A method of correlating heat-transfer data for surface boiling of liquids. Trans. Am. Soc. Civ. Eng. **74**, 969–975 (1952). https://doi.org/10.1115/1.4015984
47. J.R. Cooper, R.B. Dooley, The International Association for the Properties of Water and Steam (Revised release on the IAPWS industrial formulation 1997 for the thermodynamic properties of water and steam), IAPWS R7-97 (2007)
48. B.P. Leonard, S. Mokhtari, Beyond first-order upwinding: the ultra-sharp alternative for non-oscillatory steady-state simulation of convection. Int. J. Numer. Methods Eng. **30**, 729–766 (1990). https://doi.org/10.1002/nme.1620300412
49. R.C. Swanson, E. Turkel, On central-difference and upwind schemes. J. Comput. Phys. **101**, 292–306 (1992)
50. K.R. Rajagopal, *Navier–Stokes Equations and Related Nonlinear Problems* (Springer, New York, 1995), pp.273–278
51. Y.C. Liang, W.Z. Lin, H.P. Lee et al., Proper orthogonal decomposition and its applications—part II: model reduction for MEMS dynamical analysis. J. Sound Vibr. **256**, 515–532 (2002). https://doi.org/10.1006/jsvi.2002.5007
52. H.H. Chi, Y.H. Wang, Y. Ma, Reduced-order with least square-finite difference method for neutron transport equation. Ann. Nucl. Energy **191**, 109914 (2023). https://doi.org/10.1016/j.anucene.2023.109914